5-16-2024

Effect of Axisymmetric Confinement on Turbulent Jets

Jerry Adjetey
University of Windsor

Effect of Axisymmetric Confinement on Turbulent Jets

By

Jerry Adjetey

A Thesis
Submitted to the Faculty of Graduate Studies
through the Department of Mechanical, Automotive and Materials Engineering
in Partial Fulfillment of the Requirements for
the Degree of Master of Applied Science
at the University of Windsor

Windsor, Ontario, Canada

2024

Effect of Axisymmetric Confinement on Turbulent Jets

by

Jerry Adjetey

APPROVED BY:

_____

N. Biswas
Department of Civil and Environmental Engineering

_____

V. Roussinova
Department of Mechanical, Automotive, and Materials Engineering

_____

R. Balachandar, Advisor
Department of Mechanical, Automotive, and Materials Engineering

April 30, 2024

DECLARATION OF ORIGINALITY

I hereby certify that I am the sole author of this thesis and that no part of this thesis has been published or submitted for publication.

I certify that, to the best of my knowledge, my thesis does not infringe upon anyone's copyright nor violate any proprietary rights and that any ideas, techniques, quotations, or any other material from the work of other people included in my thesis, published or otherwise, are fully acknowledged in accordance with the standard referencing practices. Furthermore, to the extent that I have included copyrighted material that surpasses the bounds of fair dealing within the meaning of the Canada Copyright Act, I certify that I have obtained a written permission from the copyright owner(s) to include such material(s) in my thesis and have included copies of such copyright clearances to my appendix.

I declare that this is a true copy of my thesis, including any final revisions, as approved by my thesis committee and the Graduate Studies office, and that this thesis has not been submitted for a higher degree to any other University or Institution.

ABSTRACT

The turbulent flow resulting from a round jet issuing into an axisymmetric confined chamber was investigated numerically using Large Eddy Simulation. The Reynolds number based on nozzle exit conditions was 3×10^4. The flow properties of the confined jet were compared to that of a free jet to examine the confinement effect under submerged conditions. To draw a conclusive argument on the effect of the confinement, the mean and turbulent quantities of both flow fields were compared. Proper Orthogonal Decomposition was also performed on the flow field to determine the structures/events with the highest contribution to the total turbulent kinetic energy. Attention was focused on how the confinement modified the coherent structures identified in the near exit region of the jet as these structures play important roles in particle transport and mixing.

The results obtained for the confined jet differ substantially from those of the free jet, both in the mean and instantaneous flow fields. These differences are attributed to the confining wall, which introduces a prominent recirculation zone between the shear layers and the confining wall. As a result, the once quiescent ambient became turbulent. The increased turbulence in the flow field produced wider mixing zones in the flow field. The Proper Orthogonal Decomposition results revealed that the contribution of the first mode to the total turbulent kinetic energy in the confined jet was three times higher than that of the free jet. The recirculation zone was identified to be the main contributor to this process. In analyzing the three-dimensional structures using the λ_2 criterion, two dominant structural modes were identified in the free jet: ring and helical modes. The eventual breakup of the free jet structures led to the formation of secondary line vortices. In the confined jet, the helical mode was absent, and the turbulent fluid hastened the breakup of the ring vortices. The interaction of the secondary line vortices with the breaking structures led to the formation of new hairpin-like vortices. These structures contributed to the further breakup of the primary ring vortices.

DEDICATION

To

God

ACKNOWLEDGEMENTS

I extend my heartfelt gratitude to Dr Ram Balcahndar, my supervisor, for the opportunity to work with him and learn from his expertise in the field of Fluid Mechanics. His unceasing advice, guidance, and patience during the course of this study were invaluable.

I would like to express my deep and sincere appreciation to Dr Kohei Fukuda for his much-needed advice and willingness to help.

I would also like to thank my colleagues for the camaraderie, coffee and lunch breaks, and intellectual discussions.

Lastly, I express my gratitude to anyone I may have inadvertently missed. Your contributions, whether big or small, have shaped this thesis.

TABLE OF CONTENTS

LIST OF TABLES

LIST OF FIGURES

1 INTRODUCTION

The effect of confinement on turbulent jets continues to gain attention in research due to their applications in numerous engineering fields such as combustion systems, cooling systems, jet pumps, etc. In combustion, for example, the existence of a recirculation zone (RZ) as a result of a confining wall is used to stabilize the flame and increase air-fuel mixing (Larsson *et al.*, 2015). A confined jet can be defined as any jet whose natural expansion is affected by limiting factors such as a wall or a free surface. A few examples of confined jets are impinging jets, surface jets, and radially confined jets, which is the focus of this study. The radial spread of the jet is limited by the confining walls onto which the jet attaches at some distance downstream of the nozzle. The presence of this confinement greatly affects the flow field in no small part due to the recirculation zone formed. A general representation of a confined jet showing the main features reported in the literature is illustrated in Figure 1.

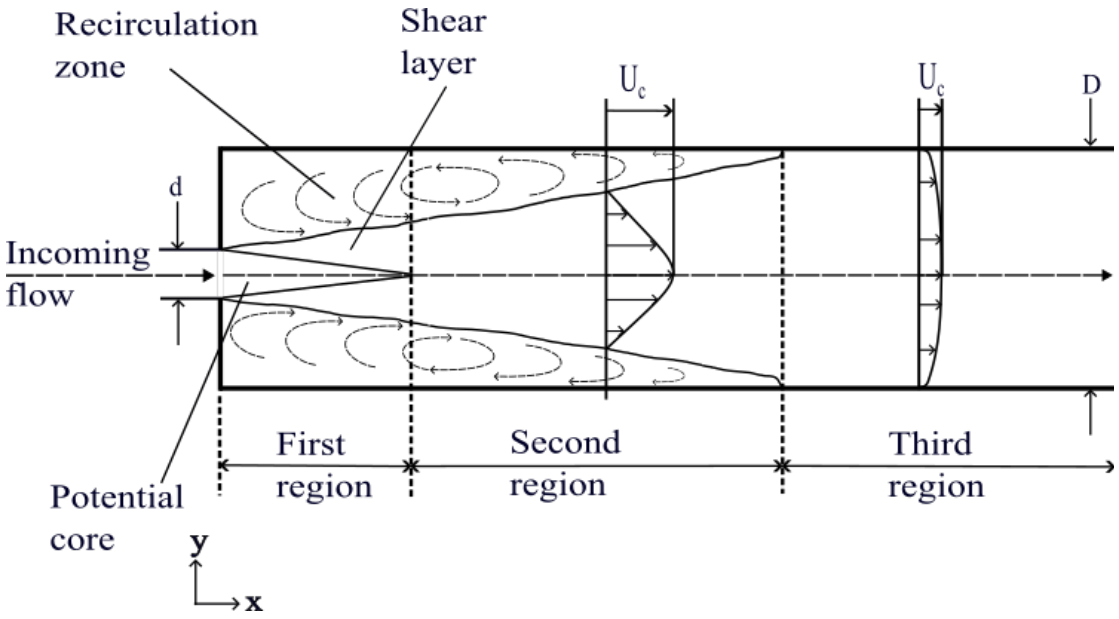

Figure 1. Schematic of a radially confined jet showing the general features of the flow field

The axial development of a confined jet can be essentially divided into three main zones as shown in Figure 1 (Liu *et al*., 1997). The first region (potential core region), similar to that of a free jet, spans the length of the potential core, where the turbulence generated in the shear layer of the jet has not yet fully penetrated the core of the jet. The properties of this region are highly affected by the turbulence characteristics of the incoming flow (Virani *et al*., 2021). Beyond the apex of the potential core is the second region wherein the axial span is dependent on the radial extent of the confining chamber. This region lasts till the point where the jet attaches to the confining wall. It should be noted that the extent of the second region can depend on the degree of confinement. For example, in the case of smaller expansion ratios Dealy, (1965) noted that the jet did not develop a self-preserving structure before attaching to the confining wall, and the second region may not exist. The third region starts at the point of attachment of the jet and the wall effect of the confining chamber becomes significant. The wall boundary layer develops as a result of the no-slip wall condition and the flow eventually becomes a pipe flow which continues to develop based on the total length of the chamber. It is once again important to note that the existence and size of each section depend on factors such as inlet condition (Reynolds number, inlet turbulence intensity, exit velocity profile) and domain size (expansion ratio, length of confinement chamber).

1.1 Mean Confinement Effect

It has been well established that the main characteristic of a free jet is the conservation of axial momentum and the self-preservation of the velocity distribution in the far-field region of the jet (Abramovic, 1963). For confined jets, the assumption of axial momentum conservation does not hold and the reason for this is explored later.

The following relation describes the self-preserving flow of free jets:

$$\frac{U_c}{U_j} = C_1 \frac{d}{x - x_o} \tag{1}$$

where d is the nozzle diameter, U_j is the jet exit velocity, U_c is the mean centerline velocity at a distance x from the nozzle, C_1 is the centerline velocity decay constant, and

x_o is the virtual origin of the jet which in most cases is assumed to coincide with the nozzle exit as a result of the uncertainty involved in predicting this distance (Rajaratnam, 1976). Different values for C_1 have been reported in literature (Albertson *et al*., 1950; Hussein *et al*., 1994). For practical purposes, a value of 6.3 has been suggested by Rajaratnam (1976). Therefore, Equation (1) can be rewritten as follows,

$$\frac{U_c}{U_j} = 6.3\frac{d}{x}. \tag{2}$$

For confined jets, the self-preservation assumption is only valid for the second region (beyond the potential core and before jet attachment to the wall) as shown by Rajaratnam (1976). For confined jets, the validity of this assumption was reported to only hold after 8 to 10 jet diameters from the nozzle (Becker *et al*.,1962). These assumptions, it should be noted, depend on factors discussed above.

According to Dealy (1965), the centerline velocity decay of a confined jet depends primarily on the nozzle diameter to pipe diameter ratio (*d*/*D*) and the jet Reynolds number. For very large Reynolds numbers, the centerline velocity decay becomes independent of the Reynolds number when considering the second region of the confined jet. Therefore, factoring in the d/D dependence as a result of the confinement effect, $f(d/D)$, Liu *et al*. (1997) modified Equation 1 to form the polynomial relation;

$$\frac{U_c}{U_j} = C_1\frac{d}{x} + C_2\left(\frac{d}{D}\right) + C_3\left(\frac{d}{D}\right)^2. \tag{3}$$

Liu *et al*. (1997) empirically determined the constants, C_2 and C_3, to be -1.4 and 0, respectively, resulting in

$$\frac{U_c}{U_j} = 6.3\frac{d}{x} - 1.4\frac{d}{D}, \tag{4}$$

and stated that this equation is only valid for circular jets. It should also be noted that the constants C_1 and C_2 are dependent on the flow conditions.

Hussein *et al*. (1994) conducted experiments to obtain up to third-order velocity moments for a free jet using different experimental techniques. Measurements were taken using

flying and stationary hot wire anemometers (FHW and SHW) and burst mode laser Doppler anemometer (LDA) in the far region of the jet ($50 \leq x/d \leq 122$). Considering the momentum balance as a function of only the centerline decay constant *B* and the half-width of the jet $r_{0.5}$, Hussein *et al*. (1994), after ignoring all second-order terms, defined

$$\frac{M}{M_o} = 2.27(r_{0.5}B)^2, \tag{5}$$

where M_o and M are the momentum flux per unit mass at the nozzle exit and any given cross-section, respectively, and B is defined as $C_1/0.5\pi^{0.5}$. The first-order contribution to the momentum integral was 106% and 85% of the source momentum for stationary hot-wire (SHW) and LDA/flying hot-wire (FHW) data, respectively. This was compared to the experimental results of Wygnanski and Fielder (1969) who reported a contribution of only 69% as a result of the loss of a significant portion of the source momentum accounted for by the mean profile. They proposed the source of this difference was due to the smaller enclosures used in earlier experimental studies. These smaller enclosures introduced recirculation between the jet and confining walls, which contributed to the reduction in the momentum of the jet (Hussein *et al.,* 1994).

Further study on confined jets was carried out by Kandakure *et al*. (2008) to determine the effect of axisymmetric confinement on the entrainment rate, jet spread rate, turbulent kinetic energy, and turbulent viscosity. They showed that a decrease in enclosure size led to an increase in the turbulent dissipation, and a reduction in turbulent viscosity, entrainment rate, and jet spread angle. The confinement led to faster decay of the jet. This was not observed by Shinneeb *et al*. (2011) who studied vertically confined jets. They observed no difference in the decay rate with increasing confinement level in the region $x/d < 50$.

The formation the of recirculation zone (RZ) in confined jet flows was investigated numerically by Doerksen *et al.* (2022) to assess the effect of diameter ratios on the critical Craya-Curtet number (H_c) below which a recirculation region will appear inside the axisymmetric chamber. They concluded that the dependence of H_c on the diameter ratio (D/d) only exists up to about D/d = 6 and reaches a constant value as the diameter

ratio increases, approaching free jet conditions. The location of the RZ is also dependent on the ratio U_2/U_1 where U_1 is the jet velocity and U_2 is the velocity of the secondary stream flowing coaxially with the jet. In the absence of secondary flow ($U_2 = 0$), the RZ is closest to the nozzle exit and moves further downstream as U_2 increases (Dealy, 1965).

The properties of the jet flow field such as entrainment and recirculation are greatly affected by the inlet conditions of the jet as reported by numerous researchers. Ashforth-Frost and Jambunath (1996) investigated the effect of inlet conditions (flat and fully developed velocity profiles) on the potential core and axial development of a turbulent axisymmetric air jet. Using LDA, they measured the mean velocity and turbulence profiles along the axis of the jet at a Reynolds number of 2.25×10^4. In terms of the effect of the inlet velocity profile, they reported that the length of the potential core, defined as the distance from the nozzle exit where the axial velocity has decreased to 95% of the initial axial velocity, was 7% higher for the fully developed velocity profile than that of the uniform inlet. This was attributed to the sharp velocity gradient that exists between the edge of the jet and the ambient fluid. This sharp velocity gradient leads to a higher rate of entrainment, hence a wider diverging angle for the mixing zone formed in the shear layer. The shear layers therefore intersect at a shorter distance (end of the potential core) for flat profiles as compared to fully developed profiles.

1.2 Flow Structures in Jets

Shademan *et al*. (2016), focusing on the near jet exit region of jet impingement on a flat surface, discussed the dynamics of the roll-up vortices created by the instabilities in the initial shear layer. They found that the roll-up vortices shed from the nozzle at a Strouhal number of 0.63 and maintained their ringlike shape up to a distance of four jet diameters from the nozzle exit. These vortices undergo transition and start to change into large-scale structures within the range $4 < x/d < 7$. Gaskin *et al*. (2023), in investigating the effect of ambient turbulence on the entrainment of fluid into a turbulent jet, noted that a turbulent ambient hastens the evolution of the structure of an axisymmetric turbulent jet. The hastened structural evolution reduces entrainment and results in the early break up of the structures. The recirculation region close to the inlet of a confined turbulent jet

effectively acts as a turbulent ambient; however, how this affects the turbulent structure of the jet has not been effectively explored.

In the study of turbulent free jets, vortical structures in both the near field and far field have been extensively studied (Cornaro *et al*., 1999; Violato and Scarano, 2013; Matsuda and Sakakibara, 2005) as they play an important role in mixing and entrainment. Previous studies have shown that free round jets have ordered vortical structures (Crow and Champagne, 1971; Hussain and Zaman, 1981; Matsuda and Sakakibara, 2005), and these structures are caused by instabilities due to factors such as increasing Reynolds number or acoustic excitation (Becker and Massaro, 1968; Crow and Champagne, 1970). Liepmann and Gharib (1992) showed that these vortical structures, as a result of the aforementioned instabilities, lead to successive rolling of the shear layers into coherent structures. Fiedler (1988) studied the coherent structures in a free jet identifying ring and helical vortices as the main vortex modules (modes) for axisymmetric jets. These structures may demonstrate different forms. At some distance from the jet exit, the initially organized structures develop three-dimensionality and either merge or break up, losing their coherence. This distance is characterized by the appearance of longitudinal vortices on the structures. The transition process to some extent depends on the turbulence level of the external stream (Wei *et al*., 1983).

Violato and Scarano (2013) described the evolution of three-dimensional structures in turbulent round jets and reported that the shedding and pairing of axisymmetric vortices led to pulsatile motions. The shedding and pairing of the vortices is followed by the growth of azimuthal instabilities as reported by Yule (1978) and Liepmann and Gharib (1992). They noted that these azimuthal instabilities (four in-plane and four out-of-plane) are responsible for the breakdown of the toroidal shape structures at the end of the potential core (Violato and Scarano, 2013). Zaouali *et al*. (2010) explored the effect of the Reynolds number on the near and intermediate field of an axisymmetric jet using LDV and concluded that decreasing the Reynolds number resulted in the extension of the near zone (the region between the jet exit and the appearance of the first wave fold) and the transition zone was displaced farther downstream. The near zone, also known as the wave-breaking length, ends at the first appearance of folds caused by shear instabilities.

Cornaro *et al*. (1992) also explored the dependence of the disturbance wavelength of the vortical structures on the Reynolds number and reported that increasing the Reynolds number leads to a short disturbance wavelength. The results reported by Cornaro *et al*. (1992) and Zaouali *et al*. (2010) are consistent with the findings of Becker and Massaro (1968) who showed that the wave-breaking length and subsequently the disturbance wavelength of the vortical structures are related to the Reynolds number by:

$$\frac{L}{d} = \frac{107}{\sqrt{Re}} \tag{6}$$

and

$$\frac{\lambda}{d} = \frac{43}{\sqrt{Re}}, \tag{7}$$

respectively, where L is the wave-breaking length, λ is the disturbance wavelength and Re is the Reynolds number. The effect of confinement on these parameters and in extension, the flow structures, to the best of the authors' knowledge are not well documented.

1.3 Need for the Present Study

The analysis of confined jets as applied to cooling and combustion applications is well explored in literature. However, the above discussion on the formation of structures in turbulent jets indicates that no studies have been conducted to understand the role of such structures in radially confined jets. The role of the structures in these applications is important in identifying ways to optimize the processes. A study at the structural level therefore provides the opportunity to explore further applications of confined jets.

This paper numerically examines using Large Eddy Simulation the effect of radial confinement on a round turbulent jet. Principally, the evolution of the vortical structures in the potential core region of a confined jet is analyzed and compared to that of a free jet. The objective is to determine what effect, if any, the confinement has on the flow structures near the jet exit and how these structures evolve downstream. The Reynolds

number considered is 3×10^4, where $Re = U_j d/v$ is calculated based on the jet exit velocity, U_j, nozzle diameter, d, and kinematic viscosity, v. The mean velocity and turbulent properties are investigated in the first two regions of the confined jet described in Figure 1. The analyses are conducted along the jet centerline and in different transverse planes at multiple distances from the nozzle exit. The evolution of the structures in the axial direction is visualized in a two-dimensional plane using the vorticity magnitude contour. To better understand the three-dimensional structure of the jets, the vortical structures close to the nozzle exit within the potential core region are identified and analyzed using λ_2 criteria. Finally, POD analysis is carried out in the vertical plane along the centerline of the jet to analyze and identify the coherent structures contributing the most kinetic energy to the flow field.

2 METHODOLOGY

2.1 Geometry

The numerical investigation of a water jet issuing into an axisymmetric confined chamber (henceforth simply referred to as chamber) is conducted in the domain shown in Figure 2. The jet is introduced through a round convergent-type contoured nozzle with an exit diameter, d, of 10 mm, which is attached to one of the ends of the chamber. The ratio of the nozzle inlet diameter to outlet diameter of the chamber (expansion ratio), D/d, is 5. Detailed nozzle description used in this simulation is available in Tandalam (2008). A constant mass flow rate of 0.23 kg/s is assigned at the nozzle inlet resulting in a jet exit velocity (U_j) of 3 m/s at the nozzle exit, which is equivalent to Re = 3×10^4 using the diameter of the nozzle exit as characteristic length. The length of the confined chamber is $50d$. Although the flow domain is axisymmetric, the cartesian coordinates are used to easily identify the planes along which flow properties were analyzed as shown in Figure 3.

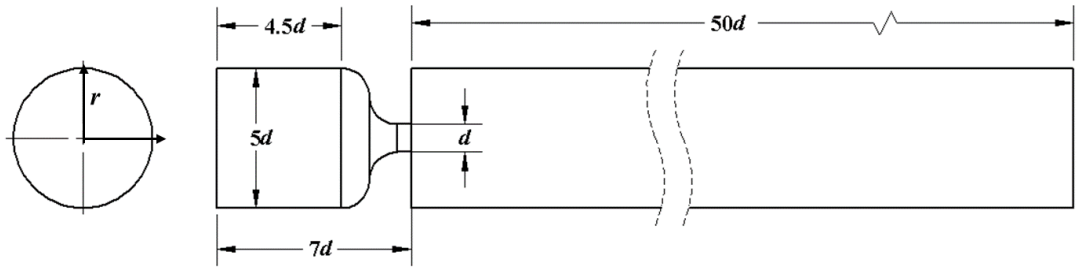

Figure 2. Schematic representation of the domain used in the simulation

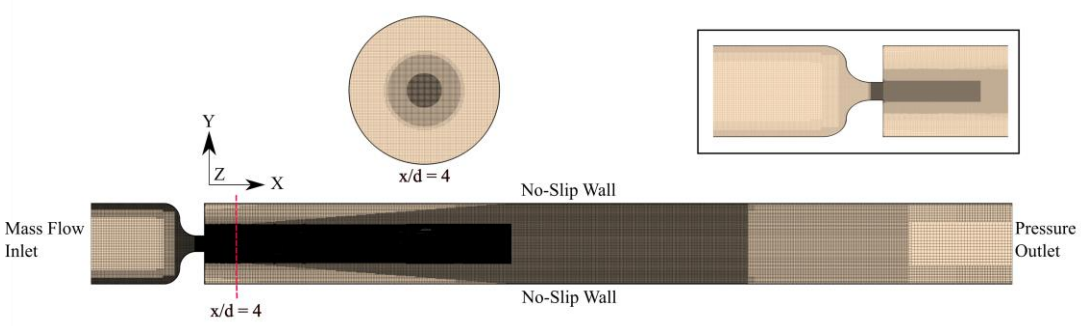

Figure 3. Mesh used for simulation showing the boundary conditions. The insets provide a closeup image of the nozzle and jet near field mesh

The computational domain and mesh used for the simulation are shown in Figures 2 and 3. Structured hexahedral mesh is used as each cell in the control volume can be subdivided anisotropically (to enhance refinements in regions of sharp velocity gradients as needed) without sacrificing mesh quality (Biswas and Strawn, 1996). The boundary conditions for the nozzle inlet and chamber outlet are mass flow inlet and pressure outlet, respectively. The confining surface is assigned a no-slip wall boundary condition. Following the studies of Celik *et al*. (2005) and Virani *et al*. (2022), both of which provide a systematic guide to be considered in generating the mesh for LES, the cell sizes are initially determined based on the Taylor microscale length scale estimated from a RANS simulation using k-ω SST and ensuring it resolved at least 80% of turbulent kinetic energy in LES. The number of cells generated in the simulation is about 8.2×10^7 cells with cell sizes ranging from as small as 0.006*d* to 0.192*d*. The smallest cell sizes are used within the converging nozzle exit and in the middle of the confined chamber along the potential core of the jet and the shear layer region on the outside of the potential core

to capture the sharp changes in the velocity gradient that is known to exist in these regions. The region of jet reattachment is also refined to capture the effect of the confined wall. Beyond the reattachment points where the flow is essentially expected to behave like a pipe flow, coarser cell sizes are used. Fine prism layers are employed at all wall boundaries to capture the boundary layer as a result of the no-slip boundary condition. Due to the need to satisfy the two criteria above, a mesh dependency study has no practical consideration in LES as the mesh size acts as the filter cutoff and hence it is not possible to define a grid-dependent mesh for LES.

2.2 Numerical Details

Commercial computational fluid dynamics software Siemens Star-CCM+ v16.06.010-R8 is used to simulate the flow field. The flow is highly three-dimensional, unsteady, and incompressible, and the resulting continuity and momentum equations as shown in Equations 8 and 9 are solved:

$$\frac{\partial \bar{u}_i}{\partial x_i} = 0 \tag{8}$$

$$\frac{\partial \bar{u}_i}{\partial t} + \bar{u}_j \frac{\partial \bar{u}_i}{\partial x_j} = -\frac{1}{\rho}\frac{\partial \bar{p}}{\partial x_i} + \frac{\partial}{\partial x_j}\left(\upsilon \frac{\partial \bar{u}_i}{\partial x_j}\right) + \frac{\partial \tau_{ij}}{\partial x_j} \tag{9}$$

where u and p represent the velocity components and pressure, respectively. The overbar on these components represents filtered quantity and this filtration enables the separation of the larger turbulent scales from the smaller turbulent length scales. Terms ρ, υ and τ_{ij} represent the pressure, kinematic viscosity, and subgrid-scale stress, respectively. The stress tensor is defined as:

$$\tau_{ij} = \frac{1}{3}\tau_{kk}\delta_{ij} - 2\mu_t \bar{S}_{ij}\,, \tag{10}$$

where δ_{ij} is the Kronecker delta function ($\delta_{ij} = 1$ when $i = j$ and $\delta_{ij} = 0$ when $i \neq j$) and $\bar{S}_{ij}$ is the rate of strain tensor for the resolved scale defined by

$$\bar{S}_{ij} = \frac{1}{2}\left(\frac{\partial \bar{u}_i}{\partial x_j} + \frac{\partial \bar{u}_j}{\partial x_i}\right). \tag{11}$$

LES allows for the explicit resolution of the large eddies in a turbulent flow while implicitly accounting for the small eddies using a subgrid-scale (SGS) model. The SGS model estimates the effect of the unresolved small turbulent length scales in the flow field. The resolution of most of the turbulent kinetic energy (TKE) in LES as compared to RANS which completely models the TKE, enables capturing more details of the flow field. For this simulation, the dynamic Smagorinsky model is used in modelling the small-scale eddies and this SGS model faithfully represents the subgrid part of the flow field. The dynamic Smagorinsky model gives the correct limiting behaviour of the turbulent stresses when approaching walls and can distinguish between laminar and turbulent flow regimes (Jordan and Ragab, 1998) as the Smagorinsky constant, C_s, vanishes in laminar flows. The choice of mesh size is directly tied to the filtering operation applied to the Navier-Stokes equation and this filtering process creates a criterion for differentiating the large and small scales within the flow.

The systematic guideline for generating LES mesh by Celik *et al*. (2005) and Virani *et al*. (2022) was indicated in the previous section. The procedures followed in this study are discussed in this section. A preliminary RANS simulation using k-ω SST turbulence model is first performed using a coarse mesh as a starting point to determine how well the mesh resolves the Taylor microscale, λ, given by

$$\lambda = \sqrt{\frac{10\upsilon k}{\varepsilon}}, \tag{12}$$

where υ, k and ε are the dynamic viscosity, turbulent kinetic energy, and dissipation rate, respectively. To ensure the entire flow field meets the Taylor microscale turbulent length resolution criteria as discussed by Celik *et al*. (2005) and Virani *et al*. (2022), mesh refinements are applied in specific regions as shown in Figure 2. The refinement is an iterative process with a function describing the ratio of the mesh size (Δ) to Taylor microscale (λ) monitored to ensure $\Delta/\lambda \leq 1$. Once this is achieved, the mesh is considered adequate for the initial run of the LES simulation.

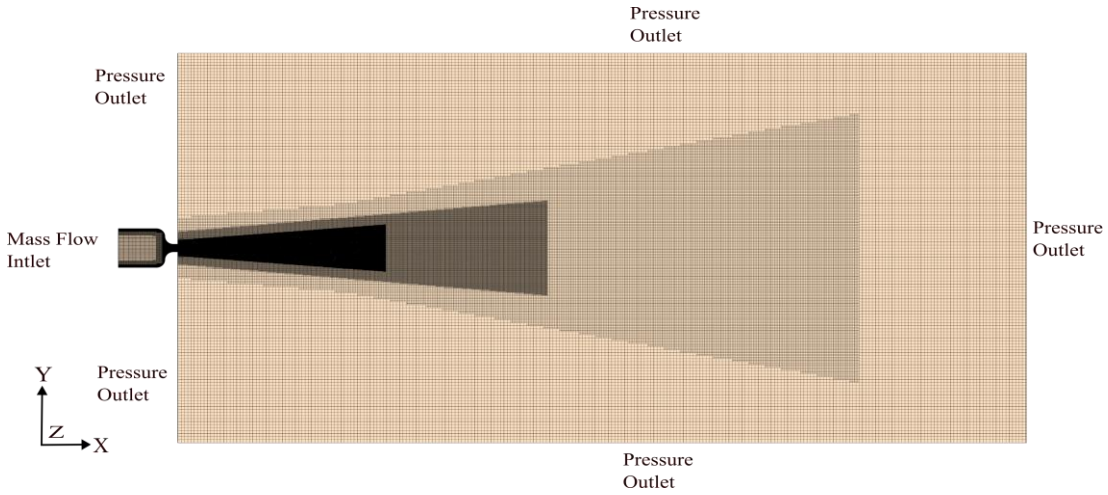

Figure 4. Mesh used for the validation case showing the boundary conditions

The final mesh and results obtained from the RANS simulation are used as initial conditions for the first attempt of LES. This helps minimize the time to reach the stable state, hence requiring fewer flow-through cycles before time-averaging for flow statistics to be started (Siemens Digital Industries Software, 2021). To confirm the suitability of the mesh for LES, the LES_IQ_k criterion is introduced where the resolved turbulent kinetic energy is compared to the total kinetic energy is checked. This is represented mathematically as,

$$LES_{IQ_k} = \frac{k^{res}}{k^{total}}, \tag{13}$$

where k^{res} is the resolved turbulent kinetic energy given by half the sum of the variances of the fluctuating velocity components (Equation 14) and k^{total} is the total turbulent kinetic energy of the flow field defined by Equation 15.

$$0.5\left[\overline{u'^2} + \overline{v'^2} + \overline{w'^2}\right] \tag{14}$$

$$k^{total} = k^{res} + k^{SGS} \tag{15}$$

where k^{SGS} is the turbulent kinetic energy modelled by the subgrid-scale model. The LES_IQ_k criterion is met a minimum LES_IQ_k of 80% throughout the domain for the present study.

The satisfaction of all the criteria discussed above makes the generated mesh adequate for the LES as it can be concluded that the target length scales are well resolved. Second order implicit scheme is used with a final time step size of 5×10^{-5} s which ensures the CFL number is less than one for the final mesh size.

2.3 Validation

Due to the lack of experimental data matching the exact conditions and domain used in the present confined jet study, the flow physics and turbulence modelling validations were performed using a submerged turbulent free jet issuing from the same nozzle (as in Figure 2) into an unconfined domain. The outer wall boundary condition in the radial direction is replaced with a pressure outlet condition and extended 25*d* radially outward away from the jet axis and the axial outlet boundary is shifted to 100*d* from the nozzle exit. This is to ensure that the boundary conditions have minimum influence on the free jet. The same inlet conditions used for the confined case are used in the present free jet simulation. The mesh used for the free jet simulation is generated following the same approach discussed in the previous section and is shown in Figure 3. The results (Figure 4) are compared to the free jet experiments performed by Tandalam *et al*. (2010) and Tian (2011) using Particle Image Velocimetry (PIV). Both experiments were performed in the same facility at a jet Reynolds number of 3×10^4 to analyze the characteristics of a free jet. Figure 4a shows the comparison of the mean streamwise velocity profiles taken at $x/d = 3$ for both LES and the experimental results of Tandalam *et al*. (2010). The mean axial velocity component (U) is normalized by the maximum local centerline velocity (U_c) while the radial distance (in the y direction) is normalized by the distance from the nozzle exit. A good agreement between the simulation and experimental results is obtained. In Figure 4b comparing the v_{rms} profile along the centerline of the jet, the LES result is in good agreement with the experimental results. The slight deviation of the v_{rms} in the near exit region ($x/d < 10$) can be attributed to the difference in the inlet turbulent

intensities of the jets as this was unreported by both Tandalam *et al*. (2010) and Tian (2011) because it is nearly impossible to measure the nozzle inlet conditions due to the limited access of the measuring instrument in that zone (Virani *et al*., 2021).

Having validated the flow physics and choice of turbulence model, the present turbulence model is used to carry out further investigation involving a turbulent round jet issuing into a confined medium.

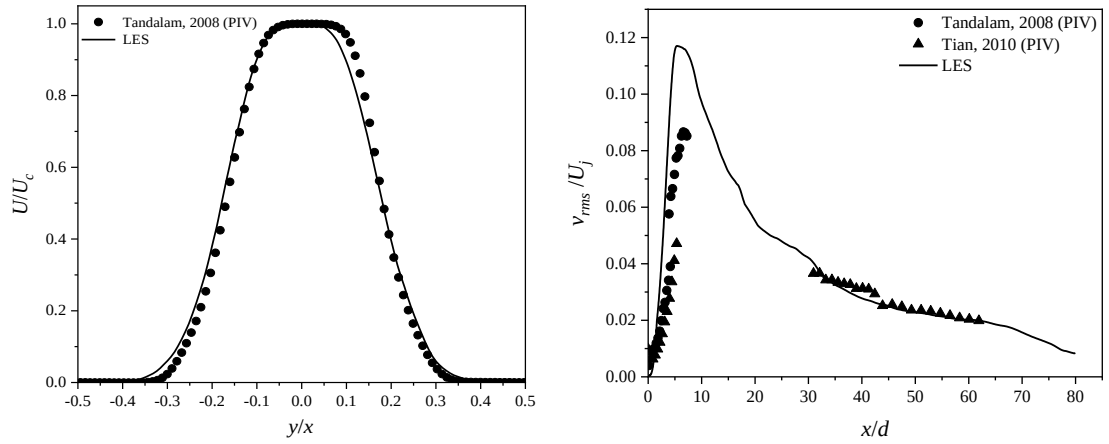

(a) (b)

Figure 5. Validation of numerical free jet case. (a) Mean streamwise velocity profile at x/d = 3 normalized by the local jet centerline velocity (U_c), compared with the experimental results of Tandalam (2008). (b) v_{rms} along the jet centerline normalized by the bulk exit velocity (U_j) compared with the experimental results of Tandalam *et al*. (2010) and Tian (2011)

3 RESULTS AND DISCUSSION

As a jet issues from the nozzle into the ambient fluid, previous studies have noted the presence of a large velocity gradient that exists between the fast-moving jet and the ambient. The velocity gradient leads to the formation of an unstable shear boundary between the two regions. Within the shear region, the instabilities result in strong velocity fluctuations, contributing to high turbulence as compared to the rest of the flow field. The high energy turbulent flow entrains the surrounding ambient fluid, promoting the growth of the shear region and subsequently affecting the flow properties of the jet. The growth

of the shear layer continues until the turbulence penetrates the core of the jet. At a distance far enough from the nozzle exit, the jet eventually dies.

3.1 Mean Flow Properties

3.1.1 Decay and Spread Rate along the Jet Centerline

One common way of quantifying the effect of different conditions on a jet is using the centerline velocity decay and the jet half-width. Figure 6a shows the decay of the centerline mean streamwise velocity normalized by the jet exit velocity, U_j for both free and confined jets. For both jets, the velocity along the centerline remains constant until $x/d \approx 5$ and experiences no decay. This defines the length of the potential core and hence the size of Region 1 in Figure 1 indicating insensitiveness to the confining wall.

For the free jet, in relation to Equation 1, C_1 is determined by taking the inverse of the slope of the line of best fit for the region beyond the potential core (Liu *et al*., 1997). In the region $5 < x/d < 9$, the centerline velocity decays gradually but no significant difference is observed between the two jets. A decay rate of $C_1 = 6.1$ is obtained for the free jet which falls within the range of values reported by other researchers (Abdel-Rahman, 2010), and a virtual origin that coincides with the nozzle exit location as suggested by Rajaratnam (1976). The decay rate also agrees well with the experimental result obtained by Tandalam *et al*. (2010) using the same Reynolds number. For the confined jet case, the centerline velocity decay rate increases exponentially with axial distance; meaning the jet decay is non-linear and continuously changes as the jet evolves downstream. The fast reduction in centerline velocity can be attributed to the changes in the ambient conditions generated by the recirculating flow due to the confinement effect accompanied by an increase in turbulence. This is also consistent with the observation of Gaskin *et al*. (2023) who noted that a jet issuing into a turbulent medium decays faster and is destroyed at a relatively shorter distance as compared to a jet issuing into a steady ambient.

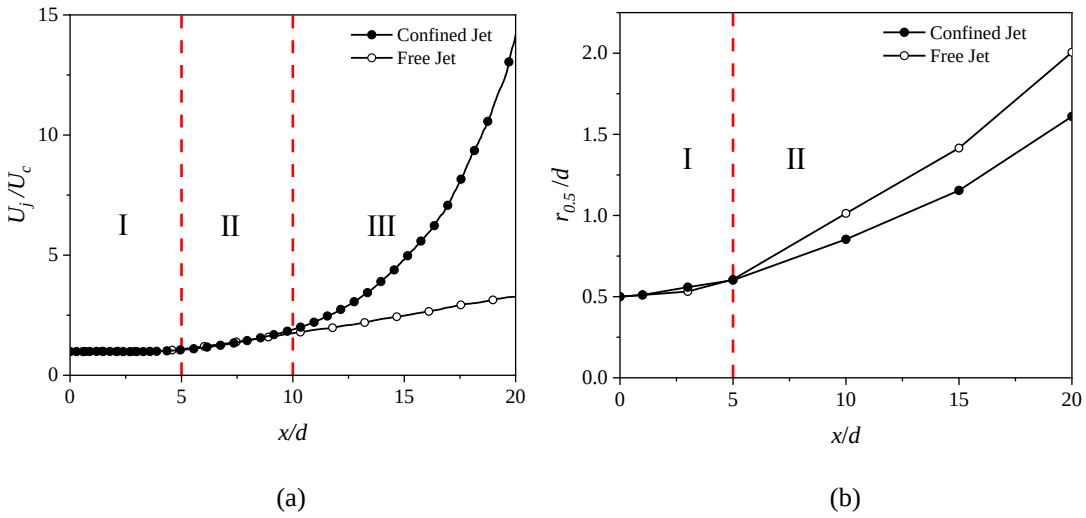

Figure 6. a) Centerline velocity decay and b) jet spread for both free and confined jets

Figure 6b shows the jet spread quantified using the half-width of the jet, $r_{0.5}$, defined as the radial location where the jet velocity is one-half of the mean centerline axial velocity at a given axial location. Due to the axisymmetric nature of the flow, the jet half-width is expected to be equal in all azimuthal directions. The slope of the half-width curve beyond the potential core signifies the spread rate of the jet. The free jet is shown to spread linearly with a growth rate of 0.092, agreeing well with 0.097 obtained by Tandalam *et al*. (2010). A reduced value of 0.067 is obtained for the confined jet and this is expected as the confinement acts to suppress the spread of the jet. Again, the confinement effect on the jet spread within Region 1 is not significant. The deviation of the confined jet case from the free jet case beyond the potential region can be attributed to the reduced entrainment of ambient fluid as the jet does not have infinite fluid to draw in as compared to the free jet. Also, the turbulence created by the resulting recirculation zone (RZ) contributes to further reducing the spread of the jet as a result of the rapid decay of the mean velocity due to a higher momentum loss, hence the growth of the jet is impacted.

3.1.2 Cross-sectional Mean Velocity Profiles

Figure 7 shows the axial velocity contour in the central vertical plane for both the confined and free jets superimposed with streamtraces. Due to the effect of the confining

wall, a recirculation zone (RZ) is developed between the outer shear boundary and the wall as reported by other researchers (Dealy, 1965; Liu *et al.*, 1997; Kandakure *et al.*, 2008). The presence of the RZ prevents the expansion of the jet resulting in lower jet half-widths with increasing axial distance as compared to the free jet as already discussed in section 3.1.1. The limiting effect of the RZ is shown in Figure 7b where the jet half-width is represented by red dashed lines. As a result of the RZ, the once quiescent ambient fluid is made turbulent, affecting the properties of the flow field.

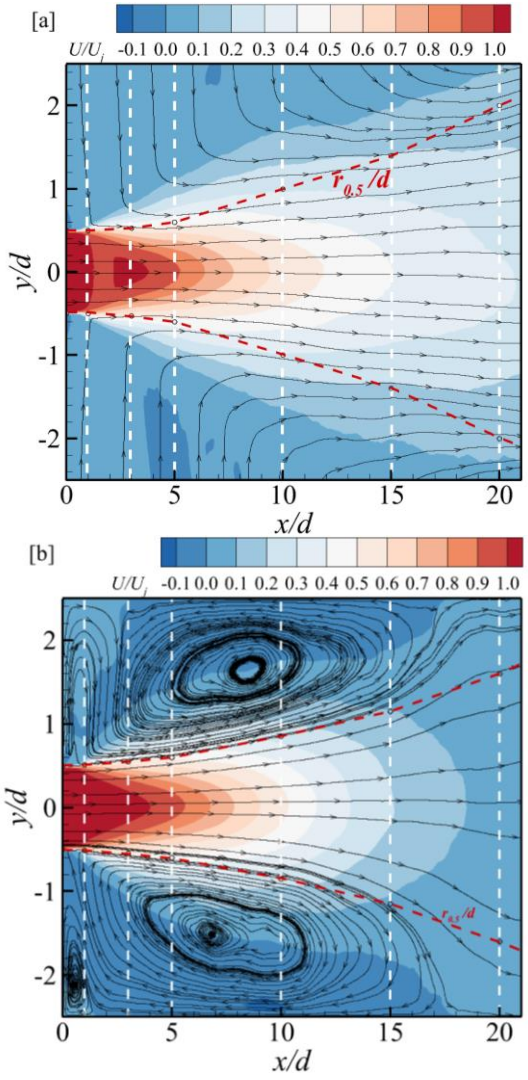

Figure 7. Streamwise velocity contour superimposed with streamtraces for a) free jet and b) confined jet clearly indicating the recirculation zone

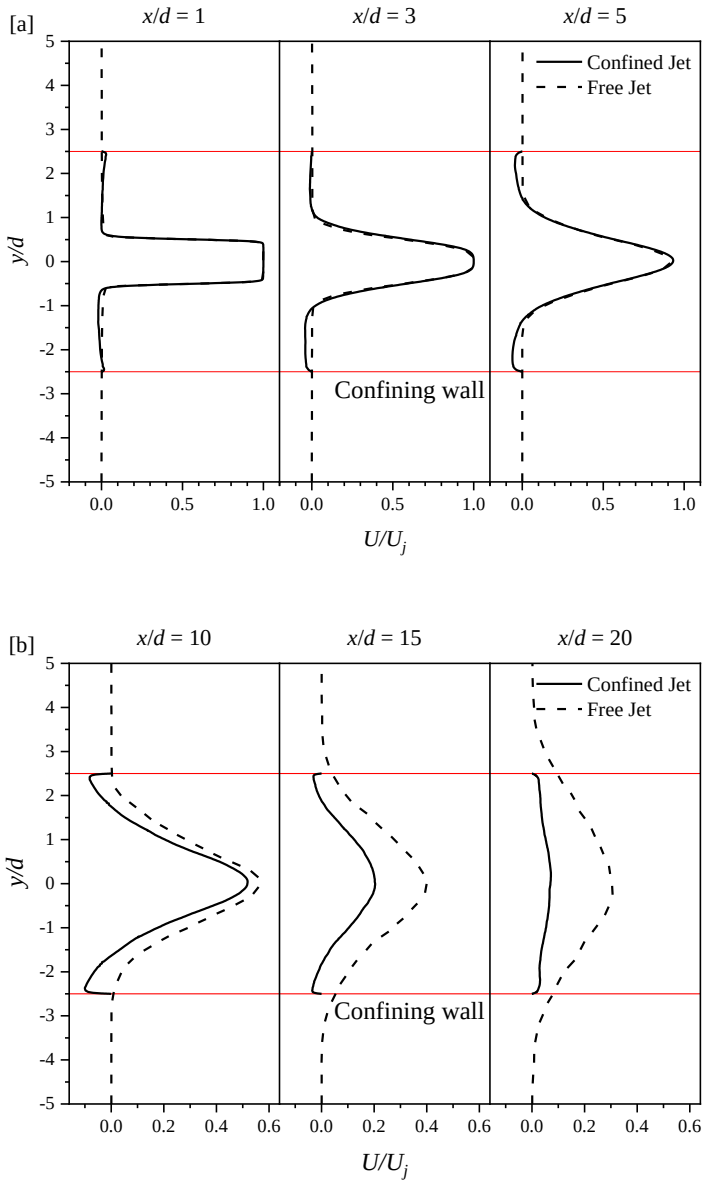

Figure 8. Axial velocity profiles in the a) first region and b) second region with solid lines at $y/d = \pm 2.5$ representing the confining wall for the confined jet case

To analyze the effect of confinement, the transverse flow characteristics are investigated at selected axial locations marked by the white dashed lines in Figure 7. Figures 8a and 8b show the axial velocity component in the first and second regions of the jets, respectively. The solid red lines represent the confining wall for the confined jet case. In Region 1, close to the nozzle exit (Figure 8a), the velocity profiles do not show any significant difference between the two cases. The reverse flow caused by the confinement

is indeed present close to the wall but not significant enough to affect the flow field. As the jet travels downstream, it is apparent from Figure 8b that the peak velocities along the centerline of the confined jet fall quickly as compared to the free jet. This is a result of the loss of momentum due to the reverse flow 'stealing' momentum from the confined jet. This conforms to the results presented for the centerline axial velocity decay in Figure 6a. In Figure 8b, at x/d = 20, the jet has already attached to the wall and the velocity profile is close to a uniform profile. The jet attachment point was determined to be x/d = 17.5 by evaluating the distribution of the wall shear stress along the confining wall and noting the crossover location where the wall shear stress switches from negative to positive.

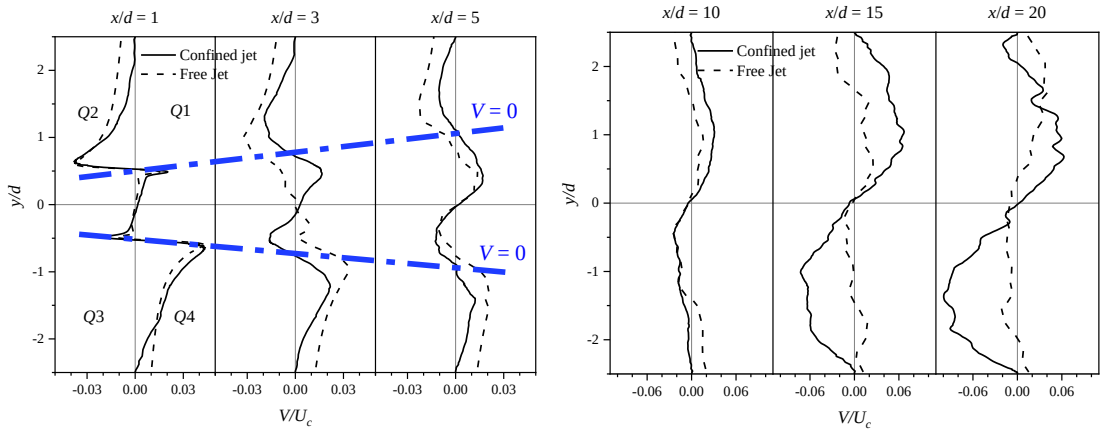

Figure 9. Radial velocity profiles in the a) first region and b) second region. The entrainment interface is indicated with blue dashed lines

The radial velocity profiles at various axial locations are indicative of the entrainment capability of the jet. In Figure 9, for each velocity profile, the data points in the first (Q1: upper right) and third quadrants (Q3: lower left) represent flow away from the jet axis (y/d = 0) while points in the second (Q2: upper left) and fourth quadrants (Q4: lower right) represent flow towards the jet axis (entrainment). Comparison of both jets at a given axial location solidifies the point that the confining wall limits the entrainment of fluid into the jet. The limiting effect of the confining wall on entrainment is further explored later. Close to the jet nozzle at x/d = 1, the entrainment interface occurs close to

the periphery of the nozzle (y/d = -0.5, 0.5) for both jets. Moving towards the wall, the entrainment of the surrounding fluid in the confined jet is suppressed as the radial velocity falls to zero. Within the first region (Figure 9a), both jets show entrainment albeit at a reduced level for the confined jet as a result of the wall. For the confined jet, it can be inferred from the graph that the entrainment interface, defined as the radial location where the radial velocity is zero (blue dashed lines), shifts from ±0.5 at x/d = 1 to ±1 at x/d =5 as the jet expands and interacts with the RZ. Moving farther downstream (Figure 9b), entrainment of fluid by the confined jet is nonexistent. The entrainment is fully suppressed by the confining wall. It should be noted that the radial velocity profiles are only indicative of the occurrence of entrainment but contain no information on the amount of fluid entrained into the jet.

Entrainment is an important aspect of jet analysis as it influences the growth of the shear layers as the jet moves downstream. For a jet discharging into a quiescent ambient, it is known that the entrainment into the jet is constant throughout downstream distance as the jet mass flow rate increases linearly and momentum is conserved. Therefore, to determine the rate of entrainment of ambient fluid into a jet, the variation of the volumetric flow rate is computed. This is done by integrating the axial velocity component (U) over the plane area (S) normal to the jet axis at specific locations downstream of the nozzle. The volumetric flow rate equation is given below:

$$Q = \int U \, dS \,. \tag{16}$$

It is important to identify the boundary of the expanding jet for entrainment computation. Due to the unsteady nature of the jet, it can be a challenge to determine the exact boundaries of the jet (full jet width) at each instance, therefore it is a common practice to define a velocity cutoff, using the time-averaged axial velocity, as a criterion (Ghasemi *et al*., 2016). Following the suggestion by Ghasemi *et al*. (2016), the entrainment of the jet is computed by integrating velocities larger than $0.003U_j$ in this study. Using Equation 16, the volumetric flow rate at different axial locations is compared to the flow rate at the nozzle exit, depicted as Q_o. The entrainment (Q/Q_o) is plotted against the axial distance as shown in Figure 10.

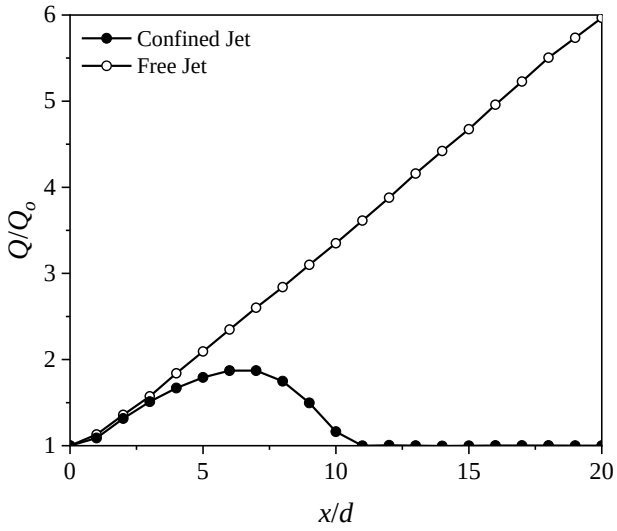

Figure 10. Entrainment

In the case of the free jet, fluid entrainment continuously increases due to the expanding shear layer and the infinite ambient fluid available for entrainment. This result differs for the confined jet as a result of the confining wall and ambient turbulence. The confined jet has a similar entrainment rate to the free jet until about $x/d = 3$. The curve then deviates from the free jet case due to a lower volume of entrained fluid as the same fluid volume is cycled throughout the domain by the recirculation zone. The entrainment peaks at about $x/d = 7$ and starts to drop until no fluid is being entrained at about $x/d = 11$. At this point, the volumetric flow is the same as the inlet flow rate at the nozzle. The location of the peak ($x/d = 7$) aligns with the center of the RZ (Figure 7a) beyond which fluid is ejected from the jet. This corroborates the radial velocity plot in Figure 9 as well as the findings reported by Kandakure *et al*. (2008).

3.1.3 Centerline Turbulence Profiles

To investigate the turbulence anisotropy along the jet centerline, the turbulence intensities (u_{rms}/U_j and v_{rms}/U_j) are plotted in Figures 11 and 12. The insets in Figures 11 and 12 represent the u_{rms}/U_c and v_{rms}/U_c profiles, respectively. From Figure 11, it is evident that the axial turbulence intensities (TI) for both jets increase gradually from zero at the nozzle exit. The u_{rms}/U_j values for the free jet case reach a peak value of 0.15 at $x/d = 6$ while the confined jet case reaches a peak value of 0.17 at $x/d \approx 7$ and plateaus for about

four jet diameters (indicated with a red dashed circle). The plateau in the region $7 < x/d < 12$ is a result of the confinement effect and this is explored further in the next section. The peak region marks the location of maximum mixing beyond the potential core. Beyond this point, the turbulence intensity values decrease as the jet travels downstream. The turbulence decay rate (slope of the curve beyond the peak) is 67% and 42% for the confined and free jets, respectively. Even though the confined jet has higher turbulence as compared to the free jet, the percentage drop in intensity shows the increasing effect of the confining wall as the jet moves downstream. A larger difference is noticed between the u_{rms}/U_j values and the v_{rms}/U_j values for the confined jet case (Figures 11 and 12) and this is consistent with literature as confinement is known to suppress the velocity fluctuations normal to the flow direction (Rahman *et al.*, 2019).

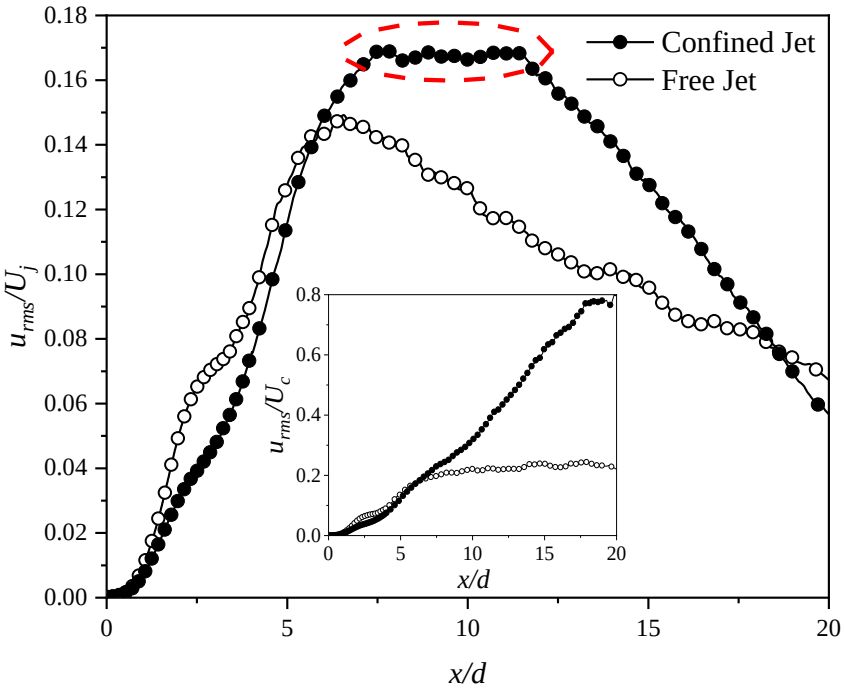

Figure 11. Variation of axial TI (inset: u_{rms}/U_c)

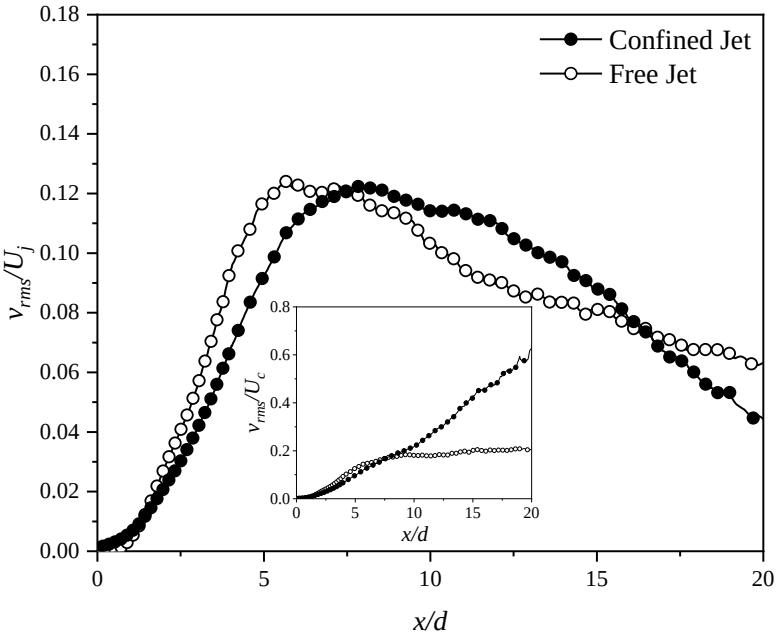

Figure 12. Variation of radial TI (inset: v_{rms}/U_c)

The u_{rms}/U_c of the free jet (Figure 11 inset) is capped at a near-constant value (asymptote) of 0.22 and compares well with values reported by Quinn and Militzer (1988) and Ghasemi *et al*. (2013). The asymptotic value is a consequence of the jet self-similarity attained within the zone of established flow (Shinneeb *et al*., 2011). Similar trends are noticed for the relative v_{rms} results in the inset of Figure 12 albeit at lower values as the flow field is dominated by the axial velocity component. For the confined jet, as the confinement effect becomes significant, the relative stresses along the centerline increase and do not achieve an asymptotic value before attachment to the wall. The relative stresses of the confined jet keep rising as a result of the fast-decaying centerline velocity (U_c) downstream of the nozzle caused by the significant effect of the confining wall.

3.1.4 Streamwise Turbulence Intensity

Figure 13 shows the streamwise turbulence intensity (TI) profiles in the transverse direction for the first and second regions (R1 and R2) of both free and confined jets. Focusing on the R1 in Figure 13a, both jets have a turbulence peak level of about 0.2 in the shear layers. The peak of the TI profiles due to shear production at the interface

between the jet and surrounding fluid widens as the shear boundary layers expand due to the entrainment of the surrounding fluid. Radially outward beyond the peaks, the rapid reduction of TI for the free jet shows a strong dissipation of the turbulence into the ambient fluid. For the confined jet, the introduction of recirculation between the shear layer and the wall (see Figure 7) leads to TI values higher than that of the free jet within that region. The TI value goes to zero at the wall because of the no-slip boundary condition. The turbulence value in the RZ increases for the confined case moving downstream of the nozzle. The increasing TI values are observed due to increasing recirculation 'chaos' towards the core of the RZ (see Figure 7a).

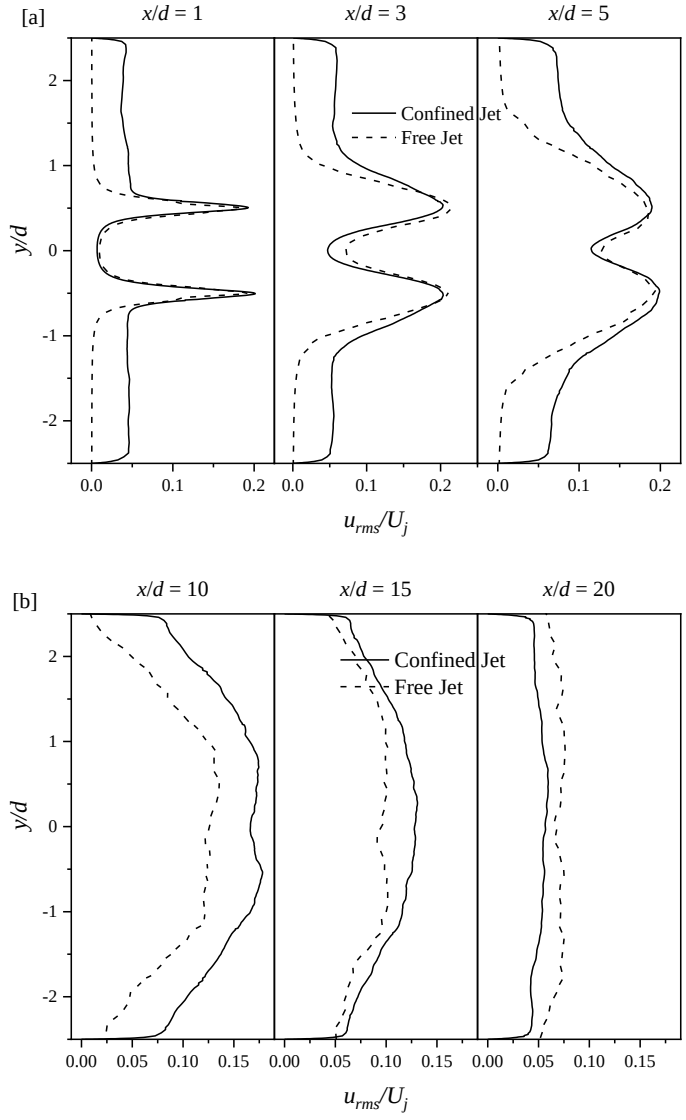

Figure 13. Streamwise turbulence intensity profiles in the a) first region and b) second region

The peak TI levels remain constant at 0.2 in the shear layers ($1 \leq x/d \leq 5$) even though the turbulence in the RZ continues to increase. At $x/d = 1$, a TI level of about 0.045 is recorded in the RZ whereas the turbulence recorded in the same region for the free jet is insignificant. Moving downstream towards the RZ core, the TI levels increase to 0.07 at $x/d = 5$, a 55% increase from $x/d = 1$. The increasing turbulence in the RZ contributes to the faster expansion of the mixing zone as the peaks widen faster in the confined jet than in the free jet. The widened mixing zone is essential for mixing applications. Contrary to the faster expansion of the mixing zone in the confined jet, the turbulence levels in the center of the jet remain similar for both jets.

The earlier development of the thicker mixing zone is linked to the faster development of three-dimensionality of the confined jet, and this is explored further in section 3.2 of this chapter. The turbulence in the RZ does not penetrate the core of the jet and has minimum effect in the R1 as shown in Figure 6a where the velocity decay rate remains constant within this region. This lack of significant difference of TI along the centerline of the jet explains why the relative u_{rms} and v_{rms} profiles remain linear and fairly equal for both jets within this region (see Figure 11 and 12 insets). As the jet travels downstream, the centerline similarity between the jets no longer holds as seen in Figure 13b.

Beyond R1, the confined jet exhibits higher turbulence levels as compared to the free jet until the jet attaches at $x/d = 18$. In Figure 13b, higher turbulence within the jet is maintained as a result of the redistribution of the RZ turbulence. This is seen in Figure 14 where the u_{rms} profiles for axial distances between $7 < x/d < 12$ are plotted. The range corresponds to the plateau region for the confined jet indicated by the red dashed circle in Figure 11. No significant difference is noted for the confined jet as compared to the free jet. The free jet experiences a gradual decrease in TI values as the dissipation of the jet turbulence into the ambient is continuous. There exists no mechanism that leads to turbulence production, unlike the confined jet where the RZ contributes significantly to the overall turbulence in the jet.

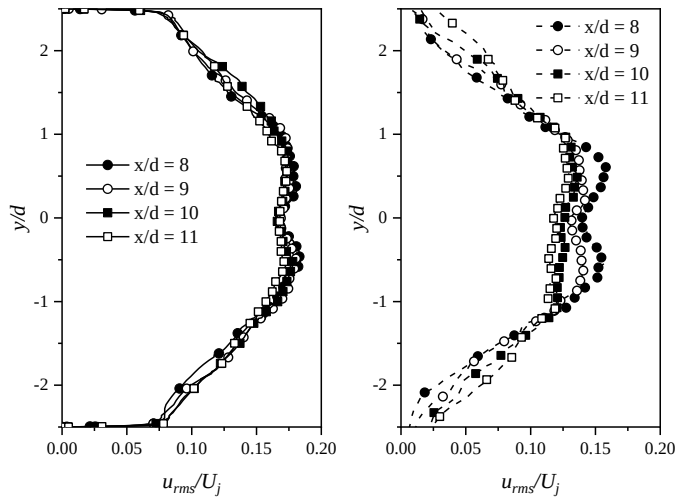

Figure 14. Turbulent intensity profiles in the range $8 \leq x/d \leq 11$ for a) confined jet and b) free jet

After the jet attachment point (x/d = 20), the free jet has higher turbulence as compared to the confined jet. At this point, the RZ no longer contributes to maintaining the high turbulence of the jet and the wall effect becomes dominant. The turbulence dissipation by the wall increases as compared to the free jet whose dissipation is only affected by increasing jet spread.

3.2 Turbulent Structures

The flow structures of a free jet are well documented in literature and these structures are known to be affected by factors such as Reynolds number and turbulence intensity. From the previous section, it has been established that the recirculation zone (RZ) exhibits strong limitations on the expansion of the jet and also makes the once quiescent ambient flow turbulent. The effect of turbulence is examined further by investigating the instantaneous flow field to reveal vortical interaction with the ambient flow.

3.2.1 Axial Shear Layer Evolution

To visualize the instantaneous jet structure near the nozzle, transverse sections were taken at different axial locations in the vicinity of the nozzle ($0 < x/d \leq 4$).

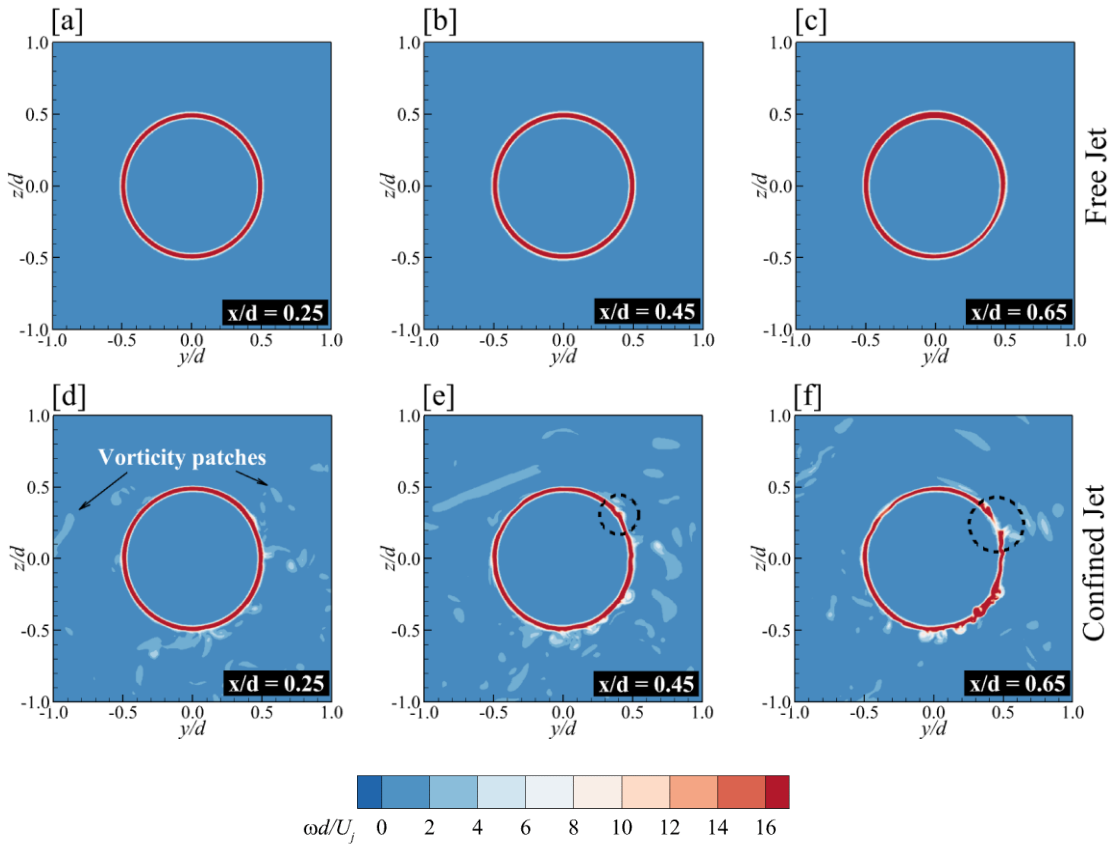

Figure 15. Shear layer deformation visualized by the instantaneous vorticity magnitude for the free (top) and confined jets (bottom) at (a, d) x/d = 0.25, (b, e) x/d = 0.45 and (c, f) x/d = 0.65

Figure 15 shows the instantaneous vorticity magnitude contours in the lateral (y-z) planes depicting the evolution of the confined and free jets. In the contours, the vorticity magnitude scale is kept the same for all locations to ensure consistent comparison. In regions close to the nozzle ($x/d \leq 0.65$), the ring vortices have a diameter similar to the nozzle exit diameter with the highest vorticity located around the ring at r/d = 0.5 in both the free and confined jets. For the confined case, the area outside the ring diameter is also accompanied by vorticity patches. The patches can be attributed to the turbulence created by the recirculation zone. In Figures 15a and d at x/d = 0.25, the ring vortices for both jets are similar as they maintain the nozzle shape. The vorticity patches attached to the outer ring of the confined jet case show the interaction of the turbulent ambient with the shear layer and hence the ring vortices. Farther from this location, in Figures 15e and f, the rings become nested with the patches along their circumference, signifying the interaction

and early deformation of the confined jet structures. At this location, the free jet structure shows no sign of vortical breakdown as the ring diameter is maintained. In Figure 15f, the deformation begins to appear on the inner surface of the ring. The appearance of the patches is later identified to be a result of the instabilities penetrating the core of the jet and interacting with the vortex rings. This is explored further in section 3.2.3. The vortex deformation on both sides of the ring enables its faster breakdown and the initial breakup point has been identified using dashed black circles in Figures 15e and f. The structural breakup is investigated in Section 3.2.3.2.

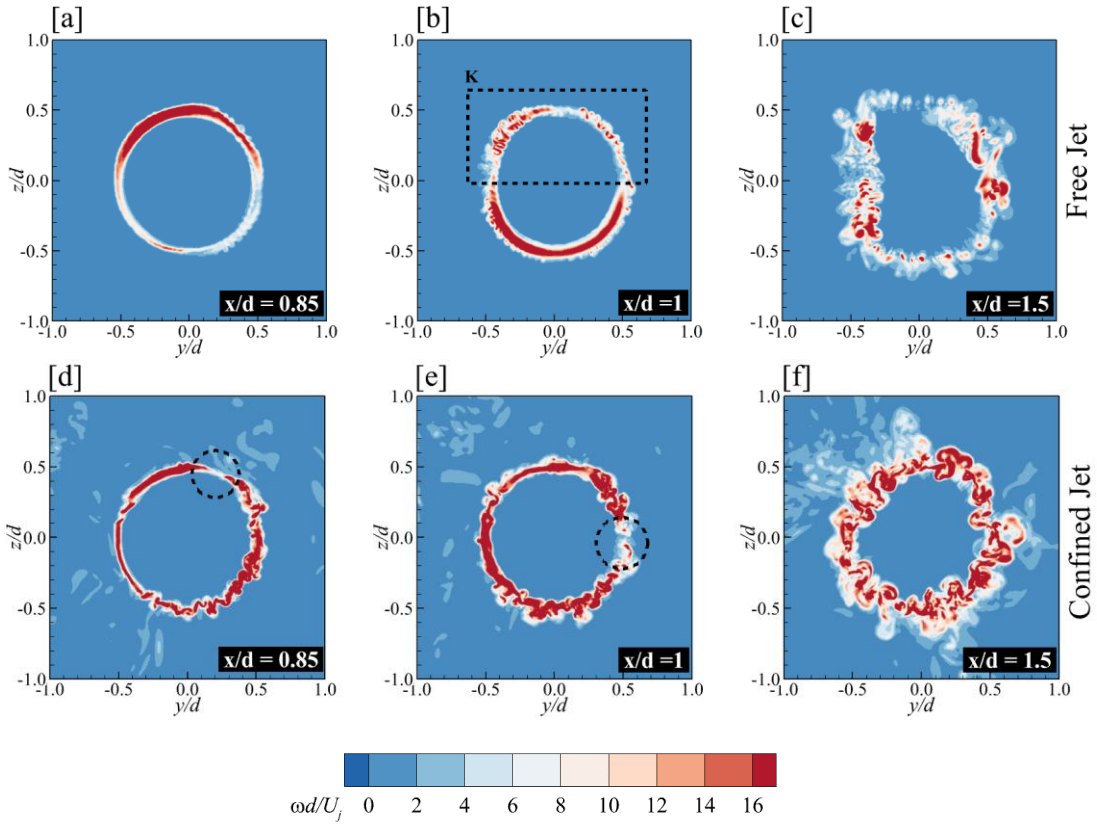

Figure 16. Shear layer deformation visualized by the instantaneous vorticity magnitude at (a, d) x/d = 0.85, (b, e) x/d = 1, and (c, f) x/d = 1.5

Figure 16 shows the continued spatial evolution of the jet shear layers in the range $0.85 \leq x/d \leq 1.5$. The vorticity magnitude contours in Figures 16a and b show a rather interesting ring structure as compared to the ones previously discussed close to the nozzle ($x/d <$ 0.85) for the free jet. High vorticity magnitude is identified in the top half of the ring in

Figure 16a with a gentle fade-out towards the bottom half. The opposite trend is seen in Figure 16b. The upper half of the structure at $x/d = 1$ exhibits a 'wavy' and distorted perimeter marked as K. The appearance of this disturbance is an indication of the onset of turbulence as the organized structures begin to disintegrate. The above-mentioned structures in Figures 16a and b can be identified to make a complete revolution when viewed together. This indicates the round ring shape is no longer persistent, but the vorticity is still concentrated along the circumference of the structure. The shape transition from $x/d = 0.85$ to $x/d = 1$ suggests a helical shape, bringing the total number of vortical modes observed in the region $x/d \leq 1$ to two: ring and helical modes. The two modes, as well as the 'wavy' perimeter, are explored in section 3.2.3. The identification of the ring and helical structures in the free jet is in agreement with the structural modes observed by Fiedler (1988). The helical mode is not observed in the confined jet as the vortical structures deform earlier, losing their coherence. Moving farther from the nozzle and adjacent to the RZ, the turbulence interacting with the jet structures intensifies leading to further distortion of the vortical rings and transition to three-dimensional structures as seen in Figures 16d and e. Beyond $x/d = 1$, the structures in the free jets transition to become large-scale eddies downstream. The transition starts early in the confined jet. At $x/d = 1.5$ (Figure 16c), the structures identified in the free jet before this point have undergone significant deformation where the organized ring shape is lost. The confined jet structures continue to break down due to the continuous interaction with the vorticity patches located within the flow field (Figure 16f).

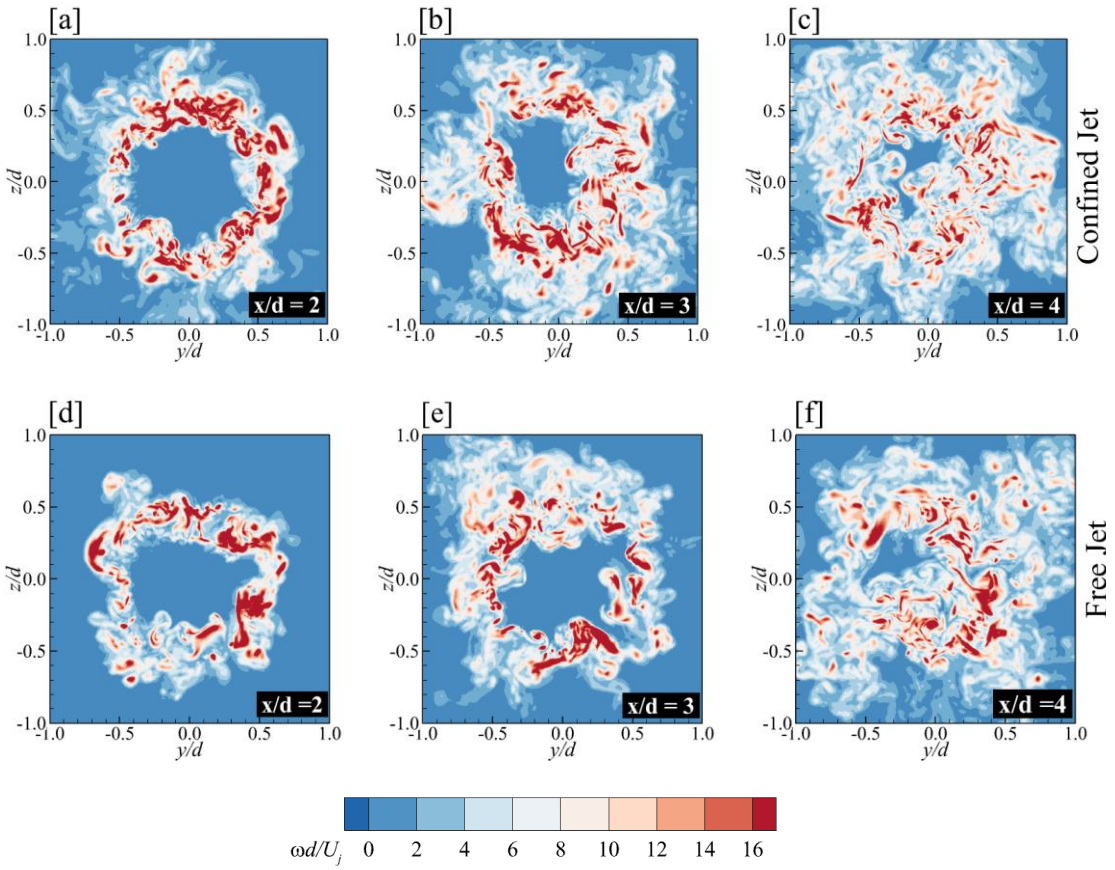

Figure 17. Shear layer deformation visualized by the instantaneous vorticity magnitude at (a, d) x/d = 2, (b, e) x/d = 3, and (c, f) x/d = 4

Figure 17 shows the further breakdown and three-dimensionality of the structures for both jets as the evolution of the jet continues downstream. At x/d = 3 and beyond, no significant difference can be identified between the two jets for the range of x/d under consideration. It is important to note that even with the early onset of the turbulence in the confined jet, the turbulence does not penetrate into the core of the jet until at about x/d = 4, the same location as that of the free jet. This agrees with the conclusion of Becker and Massaro (1968) who noted that the potential core for high jet Reynolds numbers persists beyond the onset of turbulence, identified at x/d = 0.45 and x/d = 1 for the free and confined jets, respectively. A developed turbulent mixing layer characterizes the region beyond the point of turbulence onset.

3.2.2 Disturbance Wavelength and Wave Breaking Length

Two prominent characterizing features of the structural pattern of jets as discussed by Becker and Massaro (1968) are; (a) the wave breaking length (L), the distance between the nozzle exit and the point where the first wave fold of the shear layer is observed, and (b) the disturbance wavelength (λ), the average distance between subsequent vortical rings. These features, depicted in Figure 18, are dependent on the Reynolds number (Becker and Massaro, 1968) and it is of interest to investigate the effect of radial confinement on these parameters.

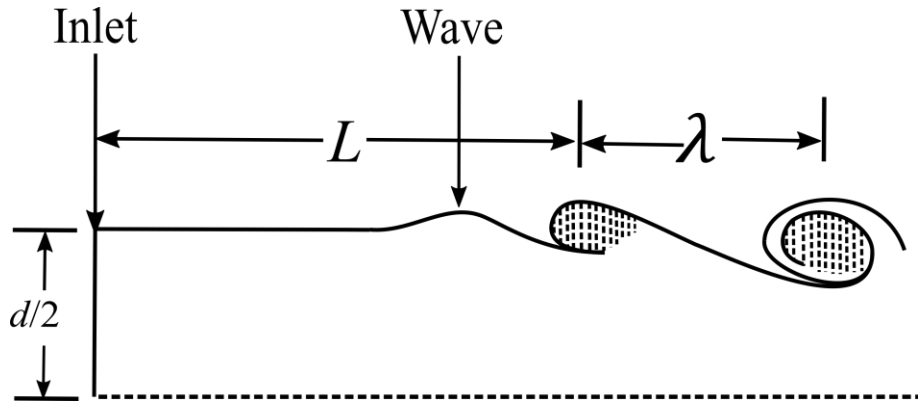

Figure 18. Pattern of shear layer evolution showing the wave breaking length (L) and disturbance wavelength (λ)

The vortex shedding process is visualized using the instantaneous vorticity magnitude contour in the x-y plane as shown in Figure 19. The initial rollup of the shear layer is caused by varicose instability as a result of increased turbulence. After one wave revolution, the leading vortex interacts with the trailing vortex, subsequently leading to vortex fusion which then dissolves into turbulent chaos. It is noted by Becker and Massaro (1968) that the cylindrical symmetry of the initial flow through the nozzle is lost immediately for jet Reynolds numbers greater than 1×10^4. A similar occurrence is observed in Figure 19 where there is no phase correlation between the shear layers past the wave disturbance length. This is clearly shown by the lack of correlation between the vortices M and N.

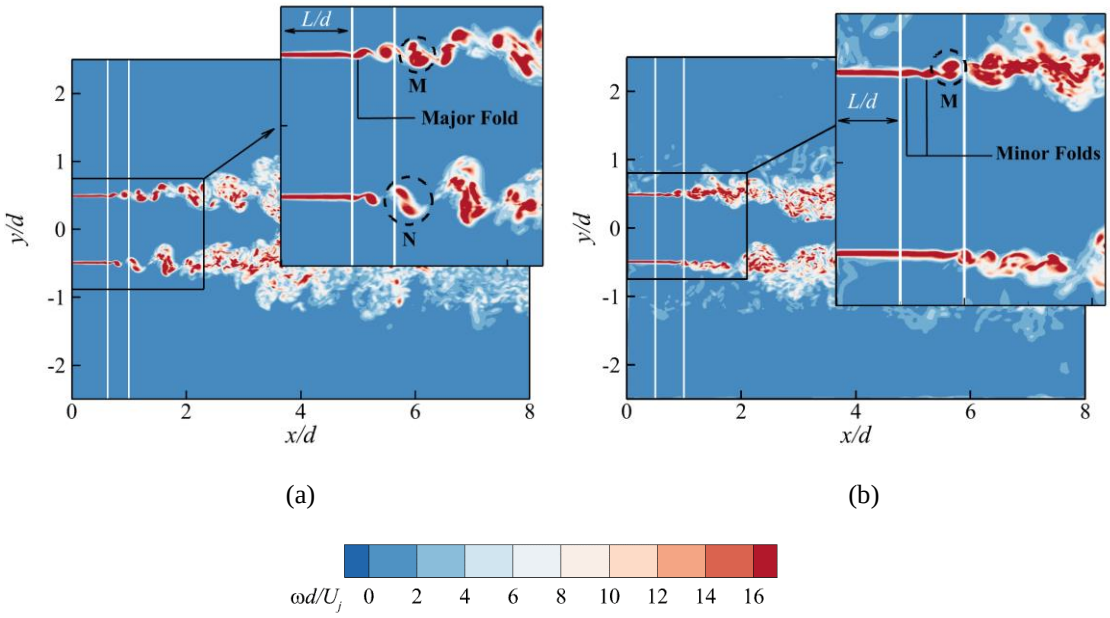

Figure 19. Shear layer deformation visualized by the instantaneous vorticity magnitude in the central *x*-*y* plane of the a) free, and b) confined jet

In this study, the disturbance wavelength and wave breaking length for both jets calculated using Equations 6 and 7 are 0.24*d* and 0.62*d*, respectively. For the free jet (Figure 19a), from the *L*/*d* line indicating the location of the first wave fold, the same value of 0.62*d* is obtained matching the theoretical value. This serves as validation for the free jet case being used as a base comparison for the confined jet. It is later shown in Figure 20 that the wavelength is 0.2*d* for the free jet, comparing favourably with the theoretical value obtained from Equation 7. The value also agrees well with the value of 0.19*d* obtained by Crow and Champagne (1971) for a free jet with a Reynolds number of 3.1×10^4.

For the confined jet, due to the earlier onset of turbulence, the first sign of wave folding appears at *L*/*d* = 0.45. This is a 27% axial distance reduction as compared to the free jet. The wave fold is not as well defined as observed in the free jet. The wave has two minor folds before fusion compared to the free jet, which experiences a complete wave revolution. The pairing process is also not well defined in the confined jet case as the three-dimensional transition occurs faster than the free jet. This contrasts with the distinct pairing process observed in the free jet shown by the black dashed circle N. For the time

instance under consideration, the turbulent ambient is shown to interfere with the wave fold and pairing of the vortices, disrupting both events. The vortices fuse at a shorter distance in the confined jet than the free jet. The fused vortices are shown by the black dashed circle M. The distance from the nozzle to the point of vortex fusion (M) is referred to as the interaction length. The interaction length for the confined jet is about $0.85d$ as compared to $1.15d$ for the free jet. This indicates the early onset of turbulence for the confined jet.

In the near region of the confined jet, the wavelength is $0.16d$ which is shorter than the $0.2d$ obtained in the free jet. The wavelength formula in Equation 6 is a function of Reynolds number, and an increase in jet Reynolds number corresponds to higher turbulence. In the case of the confined jet, as explored in Figure 9, the recirculation introduces more turbulence between the shear layers and the confining wall. The increased turbulence enhances the earlier onset of vortex breakup compared to the free jet. This leads to an increased number of rings in the region $x/d \leq 1$ for the confined jet, resulting in a shorter wavelength as the distance between two subsequent folds is reduced.

From the two-dimensional analysis of the shear layer evolution, it has been established that indeed the flow field close to the nozzle is affected by the radial confinement as a result of the RZ. The turbulence leads to the early roll-up of the shear layers and turbulence structures that interact with the shear layers leading to early vortex breakdown. These observations are explored further by examining the three-dimensional evolution of vortices.

3.2.3 Three-dimensional Flow Visualization: λ_2

There are several vortex core identification algorithms used in the three-dimensional visualization of flow structures such as Q-criterion and λ_2 criterion. In this work, the λ_2 criterion developed by Jeong and Hussain (1995), which takes into account the local pressure minima at the vortex core identified based on the flow kinematics is used. In arriving at the algorithm for the λ_2 criterion, the symmetric part of the gradient of the

Navier-Stokes equations is considered in the criterion and the resulting equation can be rewritten as

$$\frac{DS_{ij}}{Dt} - \nu S_{ij,kk} + S_{ik}S_{jk} + \Omega_{ki}\Omega_{kj} = -\frac{1}{\rho}P_{ij}, \quad (17)$$

where S_{ij} and Ω_{ij} are the shear strain and rotation tensor, respectively, defined as

$$S_{ij} = \frac{1}{2}\left(U_{i,j} + U_{j.i}\right) \quad (18)$$

$$\Omega_{ij} = \frac{1}{2}\left(U_{i,j} + U_{j.i}\right). \quad (19)$$

$U_{i,j}$ is the velocity gradient of velocity U_i taking the spatial derivative in *j*-coordinate. In simplifying the equation, the first and second terms representing the unsteady irrotational straining and viscous effects, respectively are ignored. The Hessian of the pressure, $-1/\rho \cdot P_{ij}$, shown on the right-hand side of Equation 17 has two negative eigenvalues when a vortex core with the local pressure minima is detected. Therefore, the vortex core is detected by two negative eigenvalues of the expression ${S_{ij}}^2 + {\Omega_{ij}}^2$ (which represents the vortical motion). The three eigenvalues; λ_1, λ_2, and λ_3 of ${S_{ij}}^2 + {\Omega_{ij}}^2$ should be such that λ_2 has a negative value in the vortex core.

3.2.3.1 Free Jet

Figure 20 represents the fluid structure organization at the nozzle of a free jet at the same time instance investigated in the previous sections. The aforementioned primary vortices (ring and helical vortices) are clearly identified by iso-surfaces of λ_2 coloured with velocity magnitude. A third type of coherent structure, line vortices, shown by red arrows, is also identified in Figure 20. The line vortices together with the ring and helical vortices form part of the fundamental elements of coherent structures in a flow (Fiedler, 1988). In the free jet, the line vortices are considered secondary vortices as their initial appearance result from increasing instabilities in the flow field.

Two different views are presented for structure visualization: a) side view and b) angled view. In Figure 20a, three different regions near the jet exit are identified as R1, R2, and R3 based on the structural organization. R1 and R2 represent the structural modes as observed by Fiedler (1988). In R1, the dominant structures are the ring vortices which maintain the diameter of the nozzle and show no signs of the development of instabilities. The wavelength between the identified structures is 0.2d and remains constant up to the point of the turbulence onset. In R2, the dominant structure is the helical vortex. The existence and size of R1 and R2 are time-dependent, and therefore either one of these regions may not exist in some time instances. A few such instances have been presented in Appendix A. At x/d = 1, line vortices appear on the outer surface of the helical vortices, marking the transition to turbulence. The appearance of the line vortices is a result of the growing azimuthal instabilities on the outer ring at that axial location, signifying the onset of turbulence. The turbulence onset distance (x/d = 1) corresponds to five wavelengths, in agreement with the results of Becker and Massaro (1968).

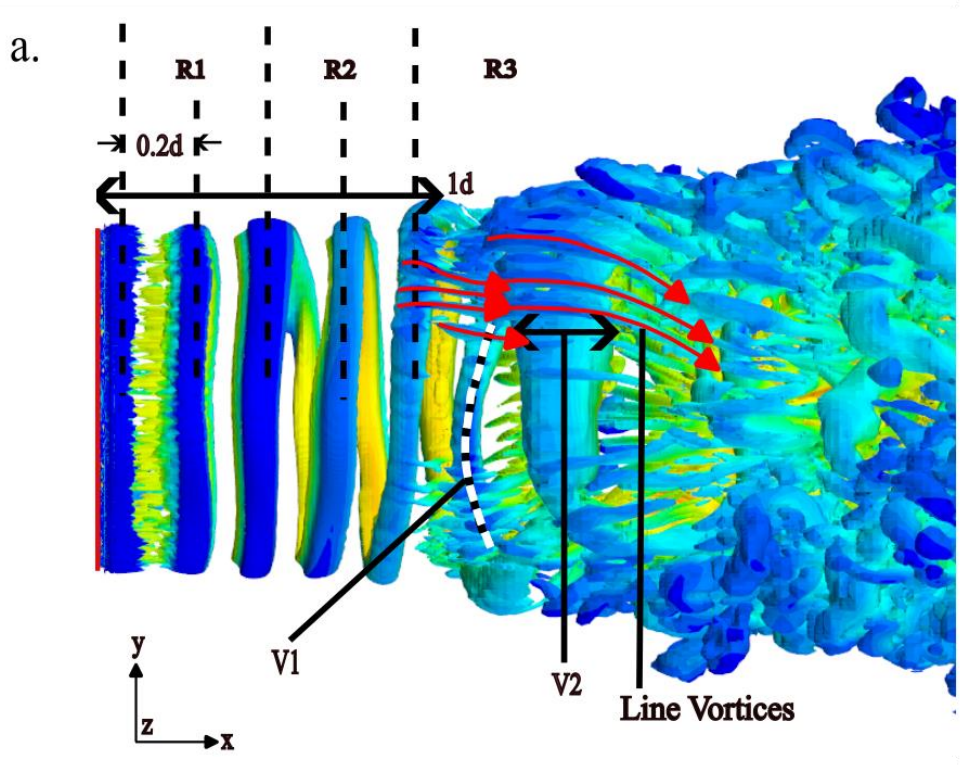

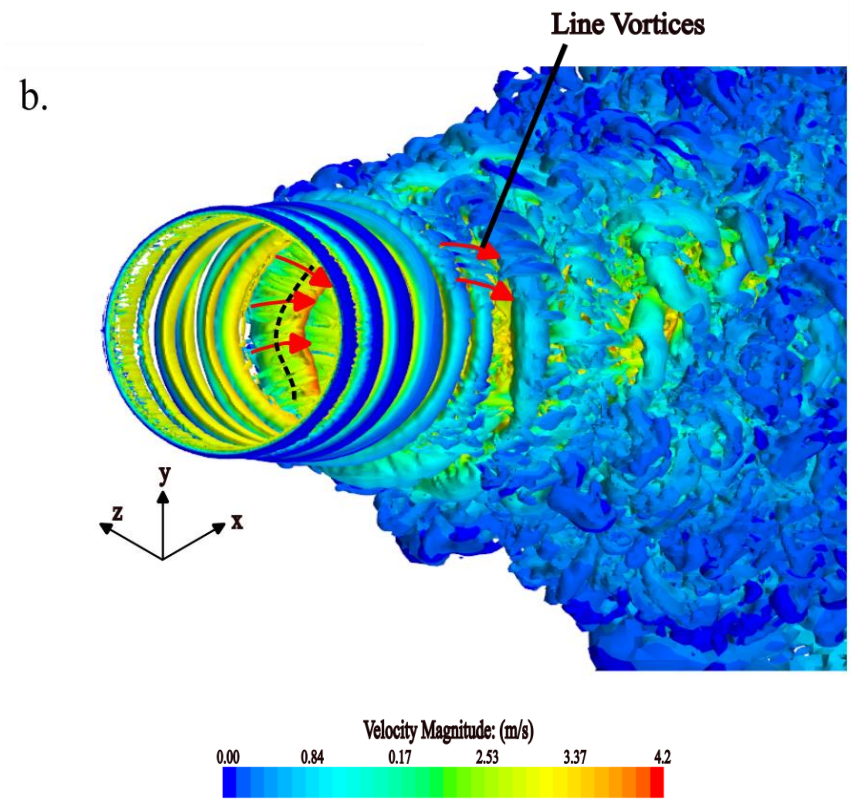

Figure 20. Instantaneous vortical structures in the near region of a free jet

Beyond x/d = 1 in R3, the line vortices (shown with red arrows) on the surface of the ring-like vortical structures stretch towards the jet core as the foremost vortex widens. The stretching of the ligaments towards the core of the jet leads to the slight shrinking of the 'pursuing' vortex. Per the Biot-Savart law (Margerit and Brancher, 2001), the induced velocity in a vortex ring is inversely related to the radius of the ring. As a result, the slightly contracted vortex, V1, has a higher induced velocity and experiences self-induced propulsion. The vortex (V1) then catches up and proceeds to either overtake the foremost vortex or merge with it. During this penetrative action, due to viscous diffusion associated with the high Reynolds number under consideration, the two rings begin to merge and propagate as a single ring. The merging of the two vortices leads to the formation of a relatively larger vortex as shown by the vortex, V2. The interaction of the line vortices with the large vortices enhances the decay of the azimuthal coherence of the fused vortical structures leading to further destruction. This conclusion was also arrived at by Violato and Acarano (2013).

3.2.3.2 Confined Jet

The spatial evolution of the confined jet is shown in Figure 21. It should be noted that in identifying these structures, a different λ_2 value is used as compared to the free jet. The small-scale structures due to the ambient turbulence in the flow field are captured by the same λ_2 value used for the free jet. This makes it difficult to identify the jet structures in the confined jet (A sample of the structures captured using the free jet λ_2 is shown in Figure A2 of Appendix A). Hence, to capture the jet structures and the effect of the turbulence on the confined jet structures, a lower λ_2 value is used. The lower λ_2 value filters out many of the small-scale structures near the nozzle exit, enabling clear identification of the dominant jet structures.

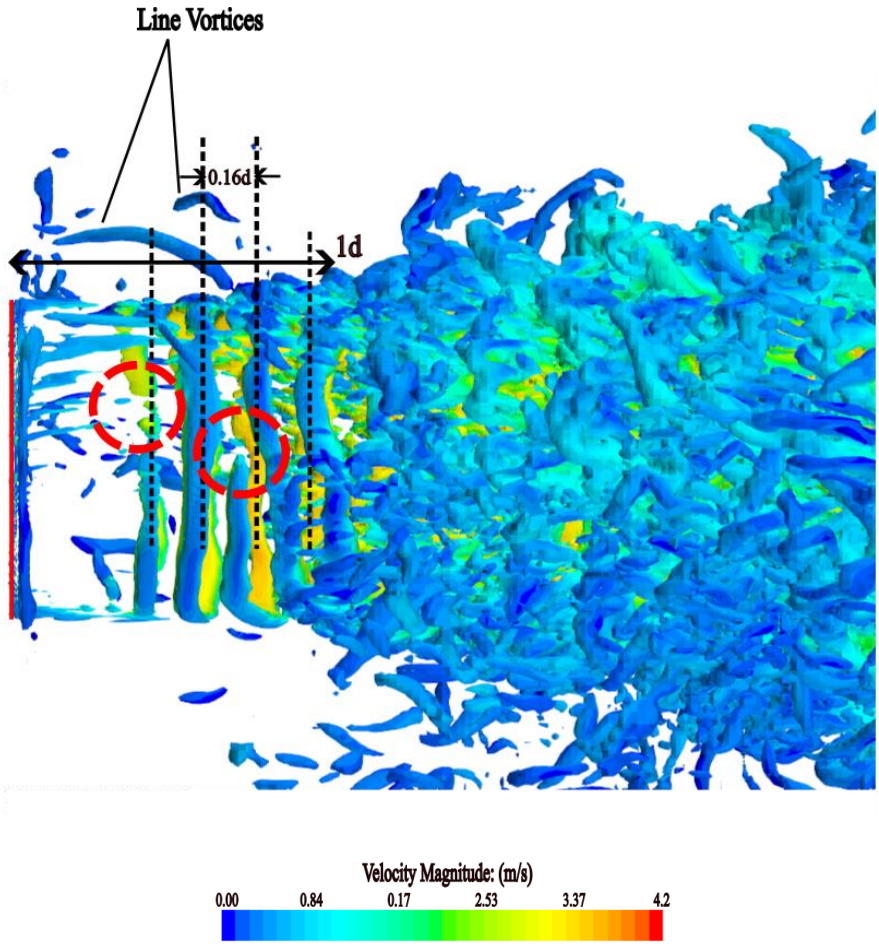

Figure 21. Instantaneous vortical structures in the near region of a confined jet – side view

From Figure 21, it is shown that turbulence transition occurs closer to the nozzle exit, aided by the ambient turbulence. The location of the turbulence onset is not clearly defined as compared to the free jet which starts after one jet diameter as reported in the previous section. There is no clearly defined region with well-organized structures similar to Regions R1 and R2 identified in the free jet. The red dashed circles highlight the breakup points in the deforming ring vortices. The breakup of the large structures into small-scale structures and the subsequent transition into turbulence enhances the mixing within the jet as compared to the free jet. The helical modes are completely absent in all instances for the confined jet.

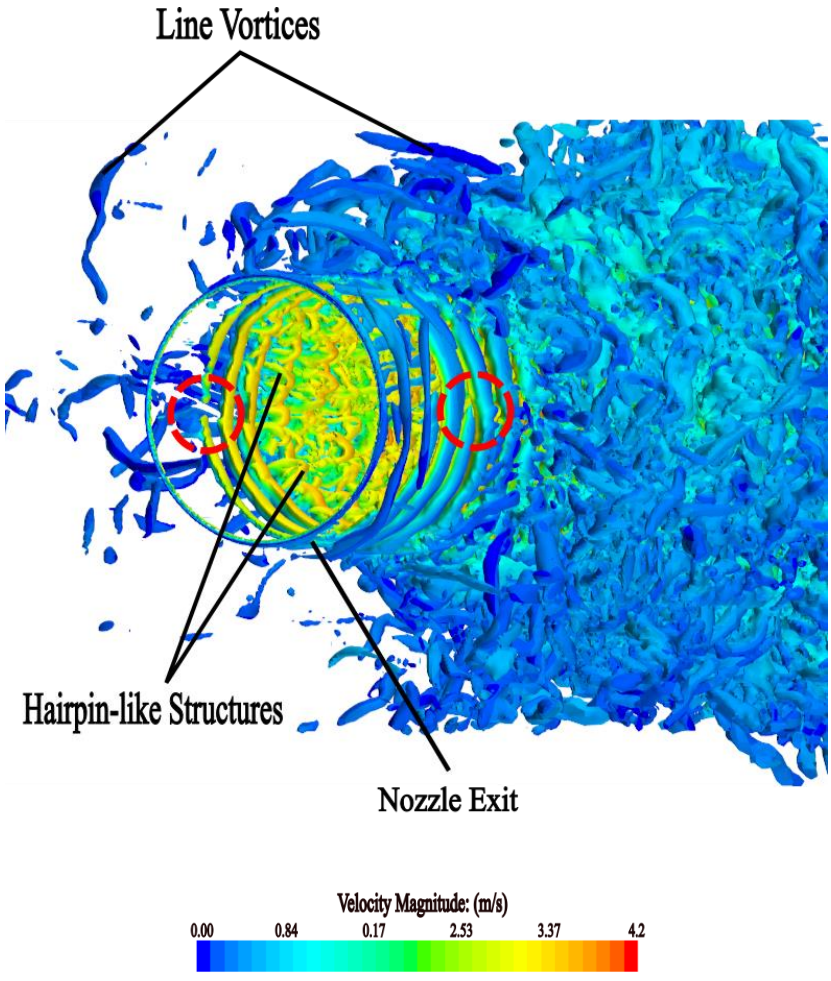

Figure 22. Instantaneous vortical structures in the near region of a confined jet – angled view

The angled view of the instantaneous three-dimensional vortical structures at the same time instance is shown in Figure 22. The discontinuity in the ring structures is clearly identified by the red dashed circles. A look inside the core of the jet shows a rather interesting new hairpin-like structures which were not observed in the free jet. These structures, just like the line vortices in the free jet, are drawn into the core of the jet. The formation of the structures may be attributed to the interaction of line vortices with the breaking structures. Figure 23 shows a close examination of the confined jet structures.

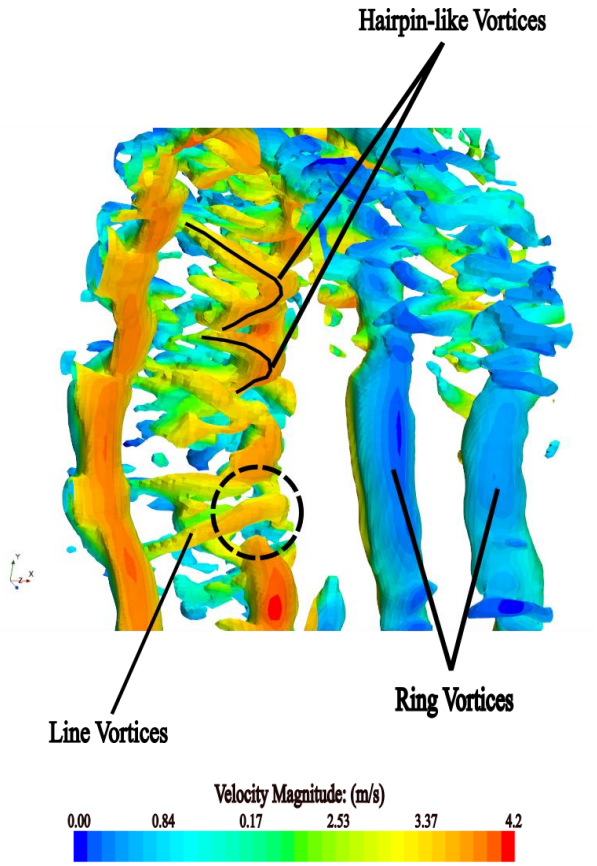

Figure 23. Instantaneous vortical structures of a confined jet – angled view ($0.7 \leq x/d \leq 1$)

Upon closer inspection of the structural organization in the range $0.7 \leq x/d \leq 1$, it is observed that not all the line vortices connect with the broken structures to form the hairpin-like structures. It is also shown in Figure 23 that the interaction of the ambient vortical structures breaks up the ring structures as highlighted in the black dashed circle lines. The secondary vortices from the rear ring contribute to breaking up the foremost

ring. The line vortices embedded between the broken ring (black circle), as well as the ring vortices, are believed to be the cause of the ring breakup. The breakup of the structures contributes to enhancing the mixing performance of confined jets.

3.3 Proper Orthogonal Decomposition (POD)

POD is used to separate the deterministic part of a flow field from the random one (Aubry, 1991). One way of achieving this is using the snapshot method. The POD modes, well described in the studies of Sirovich (1987) and Shinneeb (2008), provide spatial information on the physical structures within the turbulent flow. The modes obtained from the snapshot method are used as filters to extract the energy-contributing structures/events ordered high-to-low in a turbulent flow field. The lower modes are known to represent large-scale coherent structures/events as they are the most energic aspects of the flow field, while the higher modes may represent small-scale or random events within the flow field. From the preliminary studies, most of the energy content associated with the flow field is concentrated in the near jet exit region. Therefore, only the range $0 \leq x/d \leq 10$ in the axial direction is considered for the following POD analysis. Also, with the width of the confining wall as the limiting factor, only the range $-2.5 \leq y/d \leq 2.5$ is considered in the radial direction for both free and confined jets. Since the interest is not to reconstruct the flow field, the magnitude of the modes is of no significance.

3.3.1 Energy Distribution

The percentage of energy distribution for the first ten modes of both the confined and free jets is presented in Table 1. Figures 24a and b represent the energy contribution by the fluctuating u and v velocity components to the flow fields, respectively. For the free jet case, the cumulative energy content of 23.2% for the dominant velocity component, u, is lower when compared to other values reported by different researchers due to variations in the Reynolds numbers. Zhang and Vanierschot (2021) attributed this to the appearance of more small-scale turbulent structures in the flow field as the Reynolds number

increases. In comparison, a higher value of 33.2% is recorded for the confined jet. The increase, at this point, is believed to be a result of the added contribution of the turbulence generated in the recirculation zone to the total flow field turbulence. The mean turbulence in RZ was earlier identified (section 3.1.3) to be about 25% of the peak turbulence in the shear layer region for the confined jet. At the same location, there was no significant turbulence contribution for the free jet.

Focusing on mode 1 (M1), the confined jet has a higher energy contribution as compared to the free jet as shown in Table 1. The 9.2% contribution to the TKE by mode 1 for the confined jet is significantly higher than that of 3.2% reported for the free jet. This suggests that even though the Reynolds number and inlet conditions are the same, the structures/events contributing the highest TKE to the flow fields are different. One of the key differences, as has been established, between the free and confined jets is the recirculation zone (RZ) which makes the confined fluid turbulent. From the plot in Figure 24a, the second mode (M2) contributes about 7.9% to the total kinetic energy, which is still significantly higher than M1 of the free jet. The relatively close energy distribution between the first two modes indicates that the first two modes of the confined jet may be capturing similar events. The representation of the same fluid structures/events by the first two modes has been reported by other researchers (Zhou *et al.*, 2022). The relation between the two modes is further explored in section 3.3.2. In Figure 24a, it is observed that beyond the fourth mode (M4), the free jet has a higher contribution than the confined jet. The energy reduction in the confined jet case indicates that there is a TKE redistribution to the higher modes beyond M4. This can be attributed to the early breakdown of the coherent structures into smaller scales as observed in the previous section.

Table 1. TKE percentage distribution for the first 10 modes

Cumulative Percentage of Flow Energy						
	First mode (%)		First 2 modes (%)		First 10 modes (%)	
	u	*v*	*u*	*v*	*u*	*v*
Free Jet	3.2	17.9	6.0	32.9	23.2	68.0
Confined Jet	9.2	1.7	17.11	3.4	33.2	13.9

The radial velocity component shows a different distribution as compared to the axial component (Figure 24b). M1 of the free jet contributes about 18% to the TKE as compared to only 1.7% for the confined jet. This is most likely due to the effect of the increased turbulence in the confined jet causing the early breakup of the large-scale structures and distributing the energy evenly in the higher modes. The contribution of the structures to the TKE is explored in the next section.

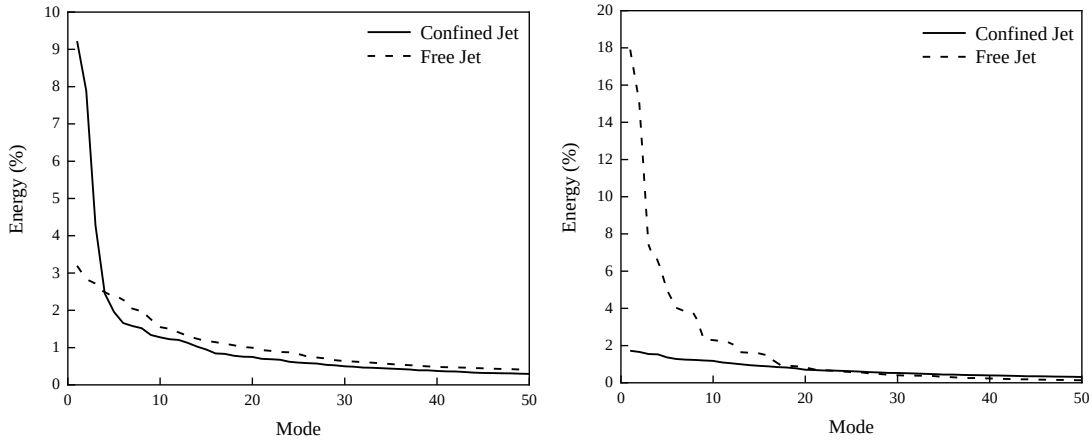

(a) (b)

Figure 24. Percentile energy distribution associated with the fluctuating a) axial, *u* and b) radial, *v* velocity components

3.3.2 Contours of POD Modes

To better understand the influence of the confining wall on the energy distribution of the flow field, contours of the first three modes are compared as they contribute the most to the total energy in the flow field. In the present study, the focus is placed on the most dominant velocity component, the axial velocity. Before focusing on the POD modes of the axial velocity component, that of the radial velocity component is briefly explored.

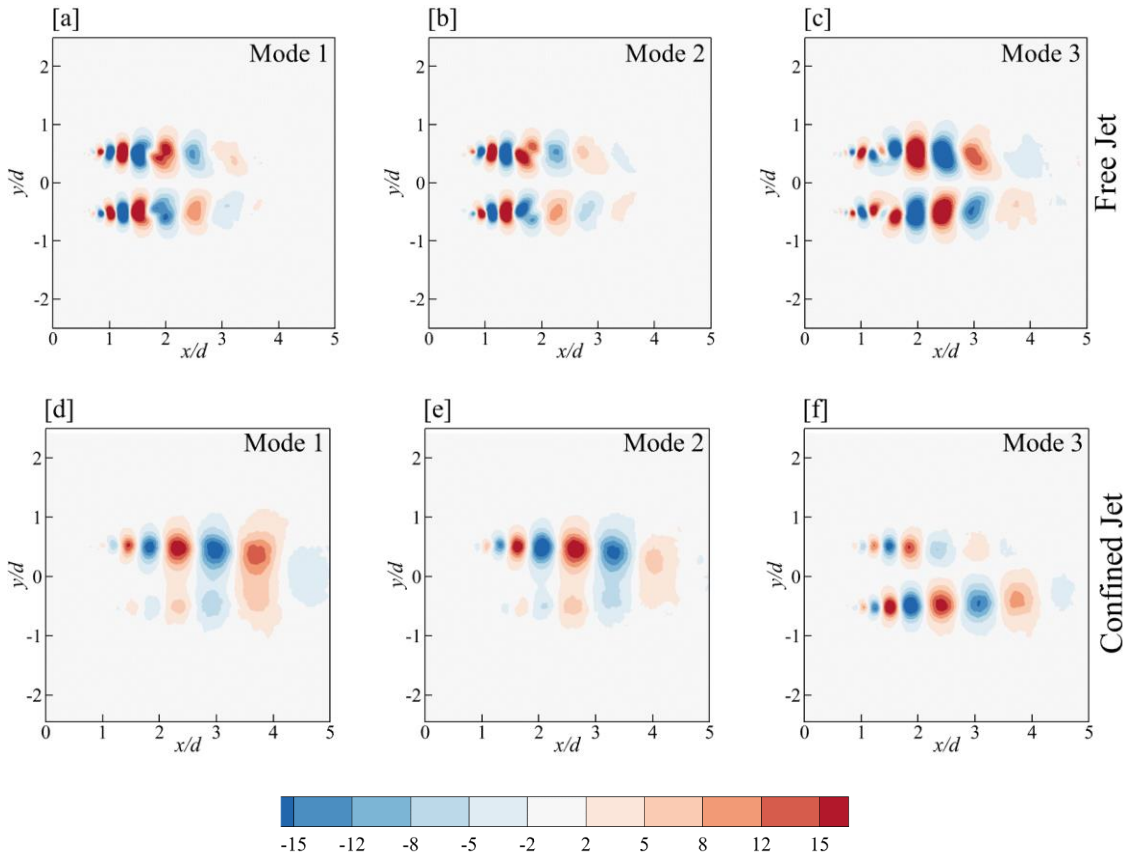

Figure 25. Contours of the first three modes (*v*) for the free (a, b, c) and confined jets (d, e, f)

Figure 25 shows the first three POD modes for the free and confined jet using the radial velocity component. As shown in the contours, the structures identified by the modes are located in the shear region of the jet. In Figures 25a, b, and c, the highly cyclical behaviour is observed in the near nozzle exit region of free jets. The modes investigated represent similar structures located within the shear layers. The main difference between subsequent modes is a phase shift which can be attributed to the periodicity of the vortex-shedding process in free jets. The phase shift in the modes represents travelling structures as they are shifted in the direction of advection (Deep *et al.*, 2022).

The modes presented for the confined jet in Figures 25d, e, and f deviate from what has been reported for the free jet. The alternating pattern observed in the free jet is not captured in the confined jet. M1 and M2 show similar patterns and can be said to be related to the same structure/phenomenon in the flow field. Since the *v* component is not

the dominating velocity component, it is a challenge to identify what the lower modes represent in the flow field. For this reason, the rest of the discussion will be focused on the axial velocity component.

Figure 26 shows the spatial patterns for the first three POD modes of the axial velocity component for both free and confined jets. In M1, the trend depicts a resemblance to the shear layer growth of the free jet. The higher magnitudes in the contour are located at x/d = 4 and beyond. The start of this region coincides with the end of the potential core where the turbulence initially penetrates into the core of the jet as the annular shear layers meet. The centerline turbulence peak was identified in Figure 6 to be located at about x/d = 6 and increased scales of the spatial structures are observed at this point. It can be concluded then that the first mode, and in extension, the second mode, captures the mixing zone beyond the potential core.

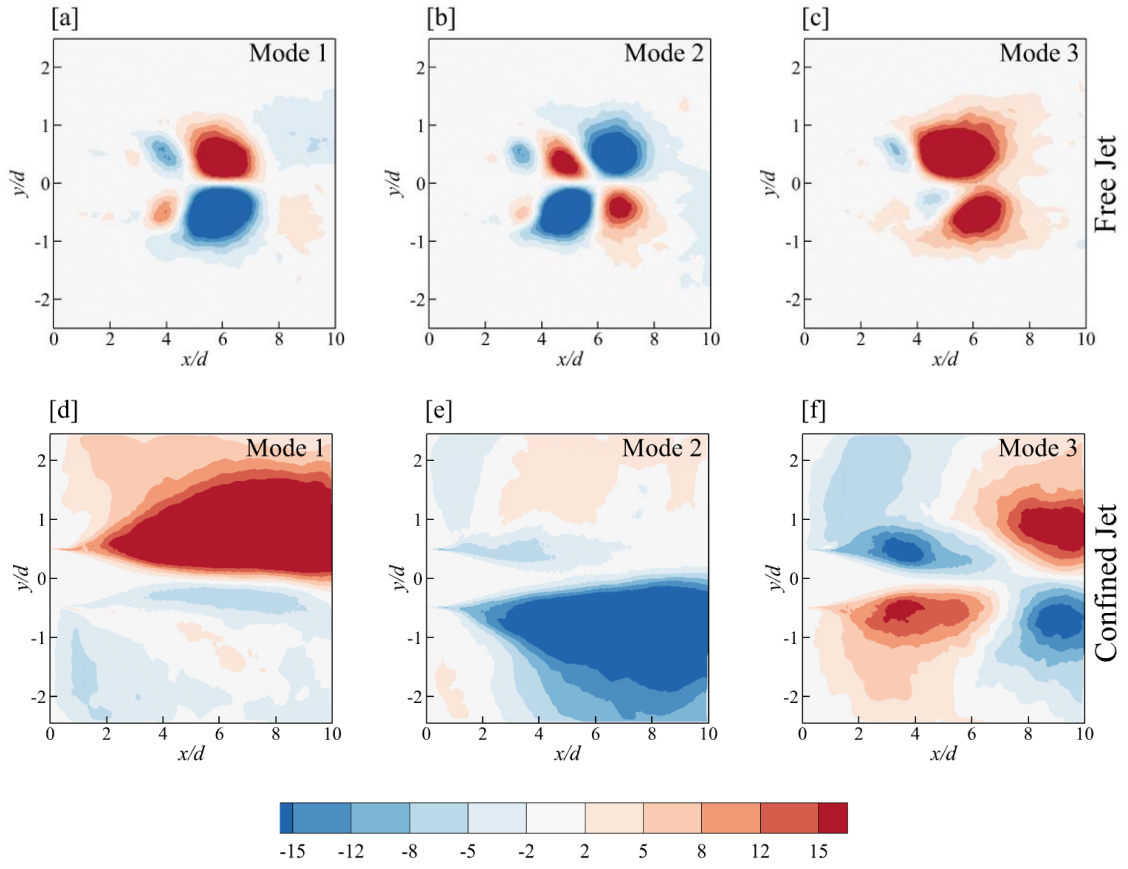

Figure 26. Contours of the first three modes (u) for the free (a, b, c) and confined jets (d, e, f).

The confined jet shows a rather interesting pattern as briefly noted while discussing the energy distribution in the earlier section. Using the same contour range used for the free jet, the one-sided appearance of the contour in M1 shows an event of interest to be investigated further. The opposite pattern is identified in M2. The two modes put together form a well-defined region of spatial structures and appear to capture the same event. The spatial pattern of the two modes is not related to the jet structures but rather represents an event. The location of the pattern suggests the event occurs between the shear layers and the confining wall. The event under investigation contributes a higher TKE percentage to the flow field as compared to other structures/events.

It has been established that the confined wall introduces a recirculation zone (RZ) which makes the once quiescent ambient fluid turbulent. From Figures 26d and e, it can be inferred that the event contributing to the spatial pattern in M1 and M2 is the recirculation zone turbulence based on the location of the patterns. In Section 3.1, the RZ was shown to contribute significantly to the total TKE in the flow field and this is reflected in the first two modes. This is similar to the observation of Shim *et al*. (2013) who attributed the irregular pattern in their M1 to the RZ formed in their planar jet experiment. In their experiment, the RZ was shown to only dominate the first mode as compared to the first two for the present study. This might be a result of the weak RZ reported by Shim *et al*. (2013). The redistribution of the RZ turbulence between the two modes can be attributed to an irregular flapping/swirling jet motion.

4 CONCLUSION

The present numerical study, using Large Eddy Simulation, focused on the effect of confinement on the flow field of a round jet issuing into an axisymmetric chamber. To quantify the effect of confinement on the flow field, the confined jet results were compared to that of a free jet. The Reynolds number, computed based on the nozzle exit conditions, was 3×10^4 and was kept constant for both jets.

The results of the analysis conducted on the two flow fields are summarized below:

- The proximity of the confining walls introduced a recirculation zone (RZ) between the shear layers of the jet and the confining wall. The recirculation zone limited the expansion of the jet and made the originally quiescent ambient turbulent.
- The turbulent ambient drastically increased the rate of centerline velocity decay. Unlike the free jet which decays linearly, the confined jet decayed exponentially, with increasing axial distance.
- The RZ turbulence contributed to increased turbulence in the flow field of the confined jet. However, due to the strong dissipative effect of the confining wall, the rate of decay of turbulence is significantly higher than that of the free jet.
- In the near region of the confined jet, the added turbulence of the RZ does not penetrate into the potential core of the jet, resulting in a potential core length similar to that of a free jet.
- The POD analysis showed that for the confined jet, the highest contributor to the total turbulent kinetic energy was the RZ which was absent in the free jet. The contribution of the first mode of the confined jet, considering the dominant velocity component, u, was three times higher than the value reported for the free jet. This signifies the recirculation zone modified the flow field.
- The effect of the recirculation zone was captured in the first two modes, while previous researchers with a weak RZ captured the process only in the first mode. This can be attributed to the strength of the RZ and the flapping motion of the jet.
- The effect of confinement on the disturbance wavelength and wave breaking length, which are functions of Reynolds number, was also discussed. The two parameters were identified to be shorter in the confined jet than that in the free jet. This showed the dependence of the two parameters on ambient turbulence.
- Investigating the near-exit region of the free jet, two dominating primary structures were identified: the ring vortices and the helical vortices. These structures, it should be noted, were well organized and easily identifiable. At about x/d =1, as a result of the increasing azimuthal instabilities on the surface of the vortical structures, secondary line vortices appeared on the primary structures.

This location marks the transition into three-dimensionality as the structures begin to lose their azimuthal coherence.

- In the confined jet, helical vortices were not observed. The ring vortices identified were not organised as they were shown to be under constant deformation and breakup as a result of the interaction between the turbulent ambient and the structures.
- A new form of secondary vortices was identified in the shape of hairpin-like vortices in the confined jet. These vortices added to the destruction of the ring vortices, contributing to the early transition into turbulence for the confined jet.
- As a result of the early transition to turbulence, confined jets are well suited for mixing applications.

REFERENCES/BIBLIOGRAPHY

Abdel-Rahman, A. (2010). A Review of effects of initial and boundary conditions on turbulent jets. *WSEAS Transactions on Fluid Mechanics, 5*(4).

Abramovich, G.N. (1963) The theory of turbulent jets. *Cambridge, MA: M.I.T. Press*.

Albertson, M. L., Dai, Y. B., Jensen, R. A., & Rouse, H., (1950). Diffusion of submerged jets. *Trans. A.S.C.E., 115*, 639-697.

Ashforth-Frost, S., & Jambunathan, K. (1996). Effect of nozzle geometry and semi-confinement on the potential core of a turbulent axisymmetric free jet. *Int. Commun. Heat Mass, 23*(2), 155–162. https://doi.org/10.1016/0735-1933(96)00001-2

Aubry, N. (1991). On the hidden beauty of the proper orthogonal decomposition. *Theoret. Comput. Fluid Dynamics, 2*, 339–352. https://doi.org/10.1007/BF00271473

Becker, H. A., Hottel, H. C., & Williams, G. C. (1962). Mixing and flow in ducted turbulent jets. *Proceedings of the 9th International Symposium on Combustion, Cornell, NY*, 7-20.

Becker, H. A., & Massaro, T. A. (1968). Vortex evolution in a round jet. *J. Fluid Mech., 31*(3), 435–448. https://doi.org/10.1017/S0022112068000248

Biswas, R., & Strawn, C. R. (1996). Mesh quality control for multiply-refined tetrahedral grids. *Appl. Numer. Math., 20*(4), 337–348. https://doi.org/10.1016/0168-9274(95)00099-2

Celik, I. B., Cehreli, Z. N., & Yavuz, I. (2005) Index of resolution quality for large eddy simulations. *J. Fluids Eng*, *127*(5), 949–958.

Cornaro, C., Fleischer, A. S., & Goldstein, R. J. (1999). Flow visualization of a round jet impinging on cylindrical surfaces. *Exp. Therm. Fluid Sci., 20*(2), 66–78. https://doi.org/10.1016/S0894-1777(99)00032-1

Crow, S. C., & Champagne, F. H. (1971). Orderly structure in jet turbulence. *J. Fluid Mech., 48*(3), 547–591. https://doi.org/10.1017/S0022112071001745

Dealy, J. M. (1964) Momentum exchange in a confined circular jet with turbulent source. [Doctoral dissertation, University of Michigan]

Deep, D., Sahasranaman, A., & Senthilkumar, S. (2022). POD analysis of the wake behind a circular cylinder with splitter plate. *Eur. J. Mech. B-Fluid, 93*, 1-12. https://doi.org/10.1016/j.euromechflu.2021.12.010

Doerksen, G., Ziade, P., Korobenko, A., & Johansen, C. (2022). A numerical investigation of recirculation in axisymmetric confined jets. *Chem. Eng. Sci.*, *254*, 155–162. https://doi.org/10.1016/j.ces.2022.117603

Fiedler, H. E. (1988). Coherent structures in turbulent flows. *Prog. Aerosp. Sci.*, *25*(3), 231–269. https://doi.org/10.1016/0376-0421(88)90001-2

Gaskin, S., Kohan, K. F., & Sahebjam, R. (2023). Reduced Entrainment into a Turbulent Jet due to Turbulence in the Ambient. *Proceedings of the 40th IAHR World Congress, Vienna, Austria*, 2170–2179. https://doi.org/10.3850/978-90-833476-1-5_iahr40wc-p0493-cd

Ghasemi, A., Roussinova, V., Barron, R. M., & Balachandar, R. (2016). Large eddy simulation of the near-field vortex dynamics in starting square jet transitioning into steady state. *Phys. Fluids*, *28*(8), 085104. https://doi.org/10.1063/1.4961199

Hussain, A. K. M. F., & Zaman, K. B. M. Q. (1981). The 'preferred mode' of the axisymmetric jet. *J. Fluid Mech.*, *110*, 39–71. https://doi.org/10.1017/S0022112081000608

Hussein, H. J., Capp, S. P., & George, W. K. (1994). Velocity measurements in a high-Reynolds-number, momentum-conserving, axisymmetric, turbulent jet. *J. Fluid Mech.*, *258*, 31–75. https://doi.org/10.1017/S002211209400323X

Jeong, J., & Hussain, F. (1995) On the identification of a vortex. *J. Fluid Mech.*, 285, 69-94

Jordan, S. A., & Ragab, S. A. (1998). A large eddy simulation of the near wake of a circular cylinder. *ASME. J. Fluids Eng*., *120*(2), 243-252. https://doi.org/10.1115/1.2820640

Kandakure, M. T., Gaikar, V. G., & Patwardhan, A. W. (2005). Hydrodynamic aspects of ejectors. *Chem. Eng. Sci.*, *60*(22), 6391–6402. https://doi.org/10.1016/j.ces.2005.04.055

Kandakure, M. T., Patkar, V. C., & Patwardhan, A. W. (2008). Characteristics of turbulent confined jets. *Chem. Eng. Process: Process Intensification*, *47*(8), 1234–1245. https://doi.org/10.1016/j.cep.2007.03.012

Larsson, I. A. S., Johansson, S. P. A., Lundström, T. S., & Marjavaara, B. D. (2015). PIV/PLIF experiments of jet mixing in a model of a rotary kiln. *Exp. Fluids*, *56*(5), 111. https://doi.org/10.1007/s00348-015-1984-9

Liepmann, D., & Gharib, M. (1992). The role of streamwise vorticity in the near-field entrainment of round jets. *J. Fluid Mech.*, *245*, 643–668. https://doi.org/10.1017/S0022112092000612

Lim, H. D., Ding, J., Shi, S., & New, T. H. (2020). Proper orthogonal decomposition analysis of near-field coherent structures associated with V-notched nozzle jets. *Exp. Therm. Fluid Sci.*, *112*, 109972. https://doi.org/10.1016/j.expthermflusci.2019.109972

Liu, H., Winoto, H. S., & Shah, A. S. (1997). Velocity measurements within confined turbulent jets: Application to cardiovalvular regurgitation. *Ann. Biomed. Eng.*, *25*, 939-948. https://doi.org/10.1016/j.expthermflusci.2019.109972

Margerit, D., & Brancher, J. P. (2001). Asymptotic expansions of the Biot-Savart law for a slender vortex with core variation. *J. Eng. Math.*, *40*, 297–313. https://doi.org/10.1023/A:1017598528328

Matsuda, T., & Sakakibara, J. (2005). On the vortical structure in a round jet. *Phys. Fluids*, *17*(2), 025106. https://doi.org/10.1063/1.1840869

Quinn W. R., & Militzer J. (1988). Experimental and numerical study of a turbulent free square jet. *Phys. Fluids*, *31*(5), 1017–1025. https://doi.org/10.1063/1.867007

Rajaratnam, N. (1976). Developments in Water Science. *Elsevier: Amsterdam, The Netherlands*, *5*.

Shademan, M., Balachandar, R., Roussinova, V., & Barron, R. (2016). Round impinging jets with relatively large stand-off distance. *Phys. Fluids*, *28*(7), 075107. https://doi.org/10.1063/1.4955167

Shim, Y. M., Sharma, R. N., & Richards, P. J. (2013). Proper orthogonal decomposition analysis of the flow field in a plane jet. *Exp. Therm. Fluid Sci.*, *51*, 37–55. https://doi.org/10.1016/j.expthermflusci.2013.06.014

Shinneeb, A. M., Balachandar, R., & Bugg, J. D. (2008). Analysis of coherent structures in the far-field region of an axisymmetric free jet identified using particle image

velocimetry and proper orthogonal decomposition. *J. Fluids Eng*, *130*(1), 011202. https://doi.org/10.1115/1.2813137

Shinneeb, A. M., Balachandar, R., & Bugg, J. D. (2011). Confinement effects in shallow-water jets. *J. Hydraul. Eng.*, *137*(3), 300–314. https://doi.org/10.1061/(ASCE)HY.1943-7900.0000306

Sirovich, L. (1987). Turbulence and the dynamics of coherent structures. I. Coherent structures. *Quart. Appl. Math.*, *45*(3), 561–571.

Tandalam, A. (2008). *Effect of Reynolds number on the characteristics of coherent structures in free round jets*. [Master's Thesis, University of Windsor]

Tandalam, A., Balachandar, R., & Barron, R. (2010). Reynolds number effects on the near-exit region of turbulent jets. *J. Hydraul. Eng.*, *136*(9), 633–641. https://doi.org/10.1061/(ASCE)HY.1943-7900.0000232

Tian, J. (2011). Free surface confinement effects on a round jet. [Master's Thesis, University of Windsor]. https://scholar.uwindsor.ca/etd/214

Violato, D., & Scarano, F. (2013). Three-dimensional vortex analysis and aeroacoustic source characterization of jet core breakdown. *Phys. Fluids*, *25*(1), 015112. https://doi.org/10.1063/1.4773444

Virani, N., Roussinova, V., & Balachandar, R. (2022). Three-dimensional turbulent jet study using volumetric particle tracking velocimetry. *12th International Symposium on Turbulence and Shear Flow Phenomena (TSFP12)*, Osaka, Japan.

Wei, Z., Niu, Z., & Ma, W., (1983). Large coherent structures in two-dimensional mixing layers. *Proceedings of the Second Asian Congress of Fluid Mechanics*, pp. 123-128. Beijing, China.

Wygnanski, I., & Fiedler, H. (1969). Some measurements in the self-preserving jet. *J. Fluid Mech.*, *38*(3), 577–612. https://doi.org/10.1017/S0022112069000358

Yule, A. J. (1978). Large scale structure in the mixing layer of a round jet. *J. Fluid Mech.*, *89*, 413–432.

Zaouali, Y., Ammar, S., Kechiche, N., Jay, J., & Ben Aissia, H. (2010). Experimental and quantitative investigation of a free round jet. *Eur. Phys. J. Appl. Phys.*, *52*(1), 11302. https://doi.org/10.1051/epjap/2010128

Zhang, Y., & Vanierschot, M. (2021). Proper orthogonal decomposition analysis of coherent motions in a turbulent annular jet. *Appl. Math. Mech*, *42*(9), 1297–1310. https://doi.org/10.1007/s10483-021-2764-8

Zhou, J., Qiu, X., Li, J., & Liu, Y. (2022). Vortex evolution of flow past the near-wall circular cylinder immersed in a flat-plate turbulent boundary layer. *Ocean Eng.*, *260*, 112011. https://doi.org/10.1016/j.oceaneng.2022.112011

APPENDICES

Appendix A: Flow Structures

The figure below shows the structures identified in the near region of a free jet. The images represent different time instances showing the different dominant structures. The first image shows the near region dominated by only ring vortices, while the second image shows only helical vortices.

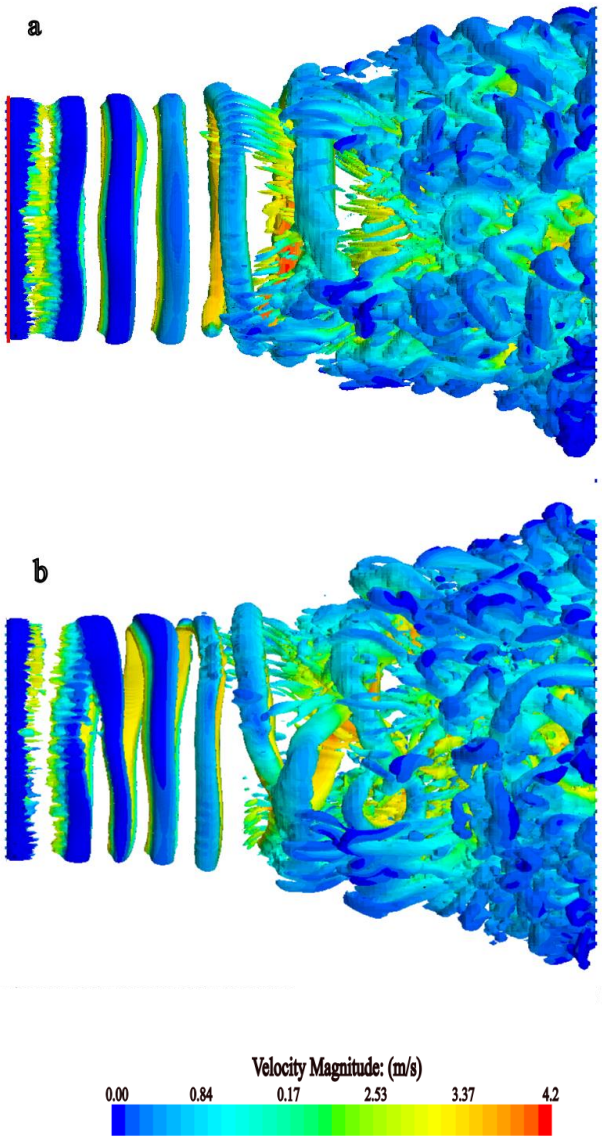

Figure A1. The near-exit region of the jet dominated by a) ring vortices, and b) helical vortices

Figure A2 shows the confined jet structures captured at the same λ_2 value used for the free jet. As a result of the ambient turbulence, many small-scale structures were captured.

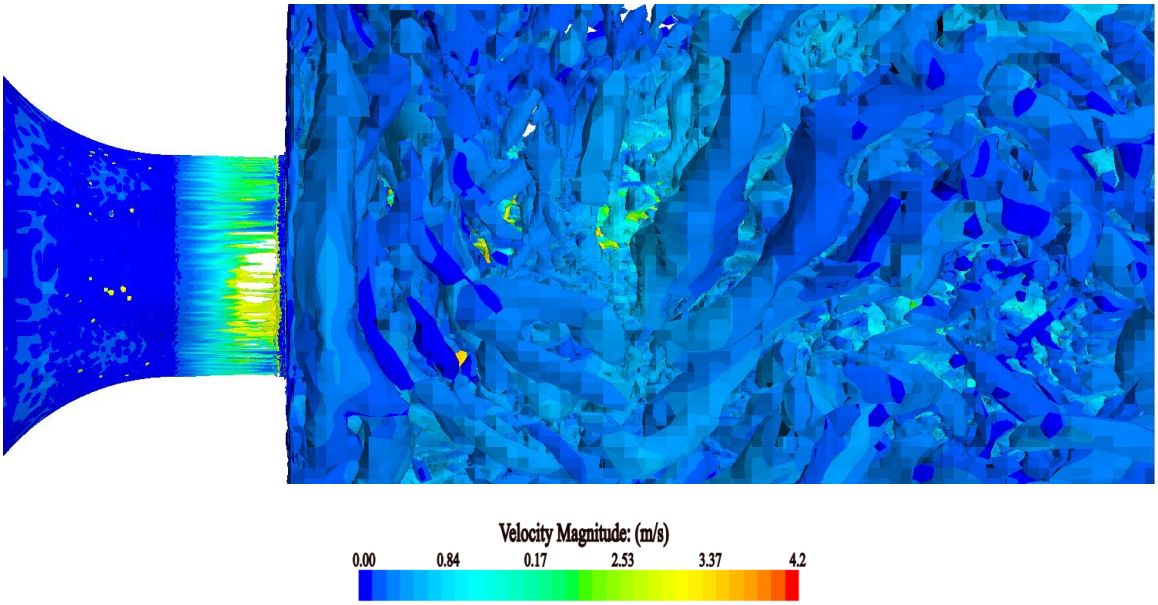

Figure A2. Confined jet structures captured using the free jet λ_2 value

VITA AUCTORIS

NAME: Jerry Adjetey

EDUCATION: Kwame Nkrumah University of Science and Technology, B.Sc., Kumasi, 2017

University of Windsor, MASc., Windsor, ON, 2024